Geophysical Journal International

Geophys. J. Int. (2015) **200,** 278–298 doi: 10.1093/gji/ggu389
GJI Seismology

A comparison of finite-difference and spectral-element methods for elastic wave propagation in media with a fluid-solid interface

Jonás D. De Basabe[1] and Mrinal K. Sen[2]

[1]*Department of Seismology, Earth Sciences Division, Centro de Investigación Científica y de Educación Superior de Ensenada (CICESE), Ensenada, BC 22860, México. E-mail: jonas@cicese.mx*
[2]*Institute for Geophysics, John A. and Katherine G. Jackson School of Geosciences, The University of Texas at Austin, Austin, TX 78758, USA*

Accepted 2014 October 6. Received 2014 October 1; in original form 2014 July 21

SUMMARY

The numerical simulation of wave propagation in media with solid and fluid layers is essential for marine seismic exploration data analysis. The numerical methods for wave propagation that are applicable to this physical settings can be broadly classified as partitioned or monolithic: The partitioned methods use separate simulations in the fluid and solid regions and explicitly satisfy the interface conditions, whereas the monolithic methods use the same method in all the domain without any special treatment of the fluid-solid interface. Despite the accuracy of the partitioned methods, the monolithic methods are more common in practice because of their convenience. In this paper, we analyse the accuracy of several monolithic methods for wave propagation in the presence of a fluid-solid interface. The analysis is based on grid-dispersion criteria and numerical examples. The methods studied here include: the classical finite-difference method (FDM) based on the second-order displacement formulation of the elastic wave equation (DFDM), the staggered-grid finite difference method (SGFDM), the velocity-stress FDM with a standard grid (VSFDM) and the spectral-element method (SEM). We observe that among these, DFDM and the first-order SEM have a large amount of grid dispersion in the fluid region which renders them impractical for this application. On the other hand, SGFDM, VSFDM and SEM of order greater or equal to 2 yield accurate results for the body waves in the fluid and solid regions if a sufficient number of nodes per wavelength is used. All of the considered methods yield limited accuracy for the surface waves because the proper boundary conditions are not incorporated into the numerical scheme. Overall, we demonstrate both by analytic treatment and numerical experiments, that a first-order velocity-stress formulation can, in general, be used in dealing with fluid-solid interfaces without using staggered grids necessarily.

Key words: Numerical solutions; Numerical approximations and analysis; Interface waves; Computational seismology; Wave propagation.

1 INTRODUCTION

The problem of modelling wave propagation in media that include solid and fluid regions has many important applications in geophysics, engineering, medicine and other areas. For example, in exploration geophysics, reflection-seismology experiments are routinely performed in marine environments, in which case the ocean constitutes the fluid region and the crust the solid one (Carcione & Helle 2004). There are many examples from engineering, one of which is the dynamic evaluation of dams (Soares Jr. & Mansur 2006; Soares Jr. 2008). An interesting application arising from the area of medicine is in clinical lithotripsy (Dahake & Gracewski 1997).

There are two types of numerical approaches that have been used in the literature to perform simulations in this medium configuration (using the classification introduced in Hou *et al.* 2012): (1) The *partitioned* approach, in which case a different equation is used in each phase and the interface boundary conditions are explicitly satisfied, and (2) the *monolithic* approach, in which case the same equation and numerical method is used everywhere in the domain and the interface boundary conditions are implicitly satisfied by letting the medium parameters change arbitrarily. One advantage of the partitioned approach is that it allows to reduce the number of degrees of freedom in the fluid subdomain, it explicitly satisfies the interface conditions and it even allows to use different numerical methods in the different phases (Stephen 1983; Dahake & Gracewski 1997;

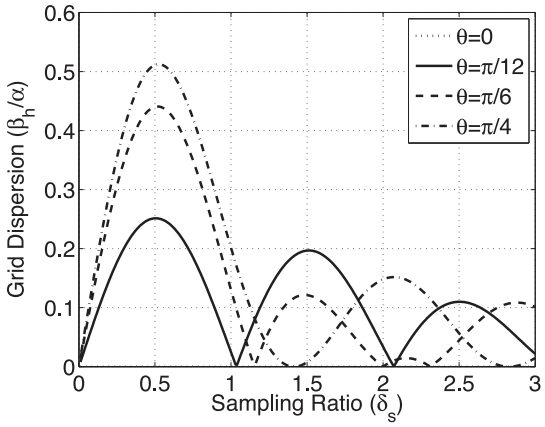

Figure 1. *S*-wave dispersion of DFDM for $\epsilon = 0$.

Komatitsch *et al.* 2000; Carcione & Helle 2004; Lombard & Piraux 2004; Soares Jr. & Mansur 2006; Käser & Dumbser 2008; Soares Jr. 2008; Madec *et al.* 2009; Wilcox *et al.* 2010; Komatitsch 2011; Qian & Yamanaka 2012). The disadvantages are that it requires precise knowledge of the location of the interface and it can be cumbersome to use if the interface has a complicated geometry. The main sought advantage of the monolithic approach is that it is easy to implement and use even for arbitrarily heterogeneous models, but the accuracy is constrained by dispersion and discretization errors (Virieux 1986; Burns & Stephen 1990; Dougherty & Stephen 1991; Stephen 1996; van Vossen *et al.* 2002). Despite the elegance and sophistication of the methods based on the partitioned approach, the monolithic approach is arguably the most common in exploration geophysics.

One clear example of the preference for the monolithic approach is the popularity of the staggered-grid finite-difference method (SGFDM), which has been known since its introduction to seismic modelling to yield accurate results at fluid-solid interfaces. In his seminal paper, Virieux (1986) demonstrated using a grid-dispersion analysis and numerical experiments that SGFDM is suitable for numerical wave propagation in media with fluid-solid interfaces without any special treatment of the discontinuity. The main outcomes of his analysis are that the *P*-wave dispersion is independent of the *S*-wave velocity, and the numerical *S*-wave velocity is proportional to the physical velocity, therefore the *S* wave vanishes in the simulations in the acoustic subdomain. This is a significant advantage of SGFDM over the standard-grid finite difference method (FDM) based on the elastic formulation of the wave equation (DFDM, Kelly *et al.* 1976), which is known for having catastrophic dispersion at this kind of interfaces (e.g. Cohen 2002).

The motivation of this paper is to study the accuracy of other monolithic methods and determine if they have catastrophic dispersion or share the advantages of SGFDM at fluid-solid interfaces. We find that a standard-grid formulation of the FDM has similar properties as SGFDM if it is based on the velocity-stress formulation of the wave equation. Furthermore, the spectral-element method (SEM) based on the displacement formulation of the wave equation can also share the advantages if the basis functions are of order two or higher.

In the next sections, we briefly introduce the numerical formulations of the elastic wave equation, their grid dispersion for the fluid-solid interface problem and the results of some numerical simulations.

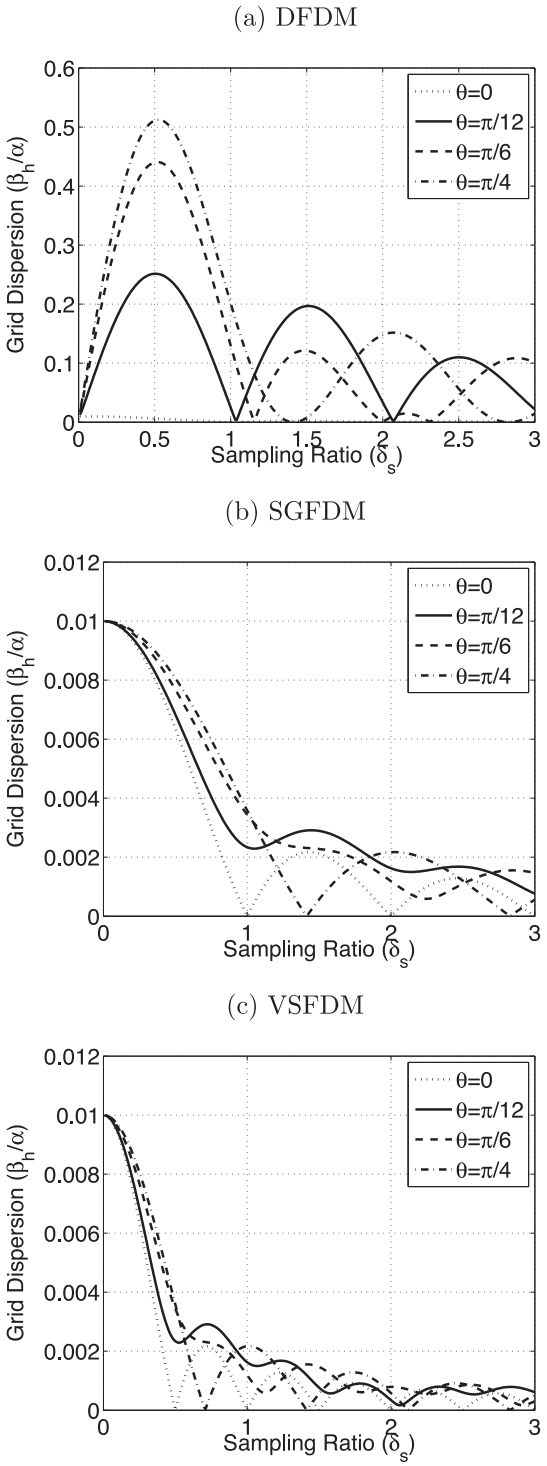

Figure 2. *S*-wave dispersion using $\epsilon = 0.01$ and (a) DFDM, (b) SGFDM and (c) VSFDM.

2 FORMULATIONS OF THE ELASTIC WAVE EQUATION

The elastic wave equation is based on the equation of motion (Aki & Richards 2002), which is given by

$$\rho \partial_t^2 u_i = \tau_{ij,j} + f_i, \tag{1}$$

where ρ is the density, u_i is the ith component of the displacement field, τ_{ij} is the i-j component of the stress tensor and f_i is the ith

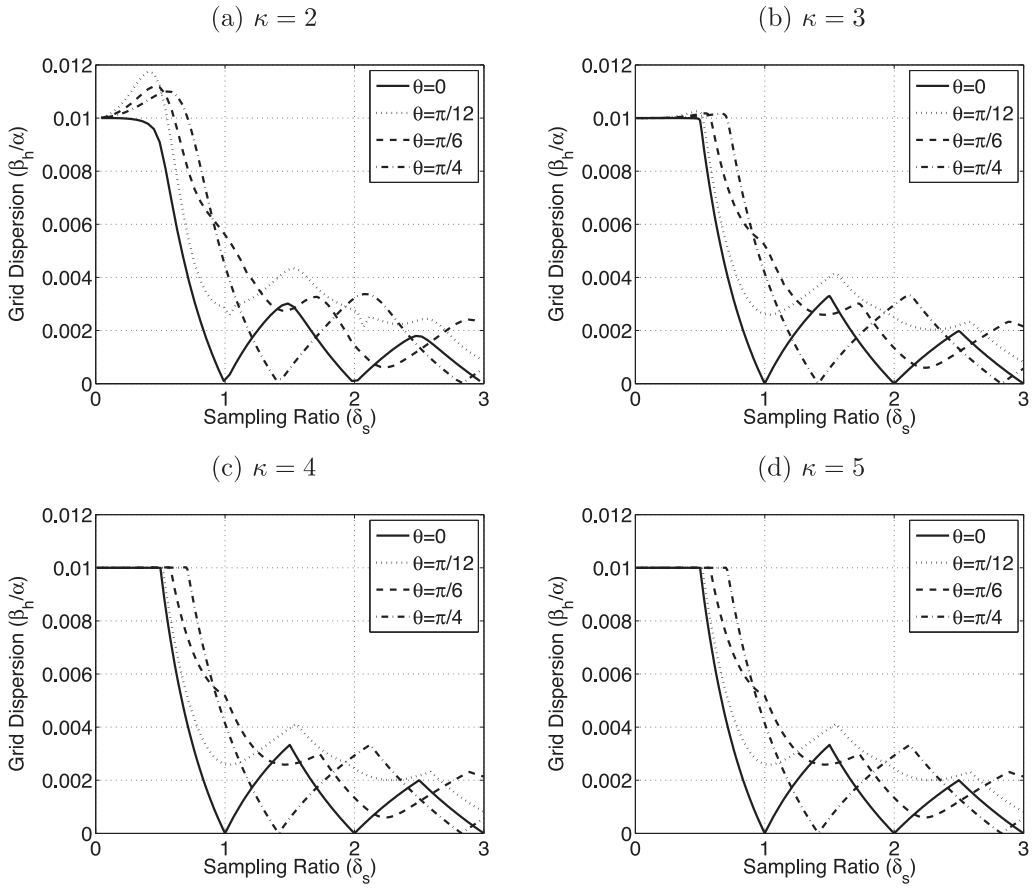

Figure 3. *S*-wave dispersion of SEM using $\epsilon = 0.01$ and (a) $\kappa = 2$, (b) $\kappa = 3$, (c) $\kappa = 4$ and (d) $\kappa = 5$.

component of the source. In the above equation and all of the following we use Einstein's summation convention unless otherwise noted. In the isotropic case, the stress tensor is related to the displacement by the generalized Hooke's law:

$$\tau_{ij} = \lambda u_{k,k}\delta_{ij} + \mu(u_{i,j} + u_{j,i}), \tag{2}$$

where δ_{ij} is Kronecker's delta and λ and μ are the Lamé parameters.

The displacement formulation of the wave equation is simply obtained by substituting Hooke's law, eq. (2), into the equation of motion, eq. (1), to yield

$$\rho\partial_t^2 u_i = (\lambda u_{j,j})_{,i} + (\mu(u_{i,j} + u_{j,i}))_{,j} + f_i. \tag{3}$$

On the other hand, the velocity-stress formulation is given by writing eq. (1) using the velocity field $v_i = \partial_t u_i$ and taking a time derivative of eq. (2), to obtain

$$\rho\partial_t v_i = \tau_{ji,j} + f_i, \tag{4}$$

$$\partial_t \tau_{ij} = \lambda v_{k,k}\delta_{ij} + \mu(v_{i,j} + v_{j,i}). \tag{5}$$

The advantage of the displacement formulation, eq. (3), is that it has a reduced number of degrees of freedom; for example, eq. (3) requires 2 degrees of freedom in each node in 2-D whereas the velocity-stress formulation of eqs (4) and (5) requires 5. Notice that these equations are typically solved numerically in time using a leap-frog scheme (regardless of the method used for the discretization in space) and therefore eq. (3) requires a minimum of four memory variables per node and eqs (4) and (5) require five per node. In 3-D and considering a leap-frog time-stepping scheme eq. (3) requires six memory variables per node and eqs (4) and (5) require nine. On the other hand, the velocity-stress formulation has the advantage of having first-order derivatives in space and in time and no derivatives on the medium parameters, which can be advantageous for some numerical methods.

The finite-element method (FEM) and related methods like SEM use the weak formulation of the wave equation which is given by the following statement: Find $\boldsymbol{u} \in \boldsymbol{H}^1(\Omega)$ such that for all $\boldsymbol{v} \in \boldsymbol{H}^1(\Omega)$

$$\left(\rho\partial_t^2\boldsymbol{u}, \boldsymbol{v}\right)_\Omega + \boldsymbol{B}_\Omega(\boldsymbol{u}, \boldsymbol{v}) = (\boldsymbol{f}, \boldsymbol{v})_\Omega, \tag{6}$$

where $\boldsymbol{H}^1(\Omega)$ is the first Sobolev space (Cohen 2002), Ω is the domain, and

$$(\boldsymbol{u}, \boldsymbol{v})_\Omega = \int_\Omega u_i v_i \, \mathrm{d}x \, \mathrm{d}z, \tag{7}$$

$$\boldsymbol{B}_\Omega(\boldsymbol{u}, \boldsymbol{v}) = \int_\Omega \left(\lambda(u_{i,i}v_{j,j} + \mu(u_{i,j} + u_{j,i})v_{i,j}\right) \mathrm{d}x \, \mathrm{d}z. \tag{8}$$

It can be shown that eq. (6) is equivalent to eq. (3) whenever a solution to the latter exists (Cohen 2002). There are many advantages of this formulation: (i) it does not have derivatives on the medium parameters, (ii) it involves only first-order derivatives on the displacement field, (iii) it has the same number of degrees of freedom as the displacement formulation of the elastic wave equation and (iv) the domain boundary conditions are implicitly satisfied. Notice that for succinctness we have assumed homogeneous Neumann boundary conditions in eq. (6) for the external boundary but other types of boundary conditions can also be accommodated; in fact, another

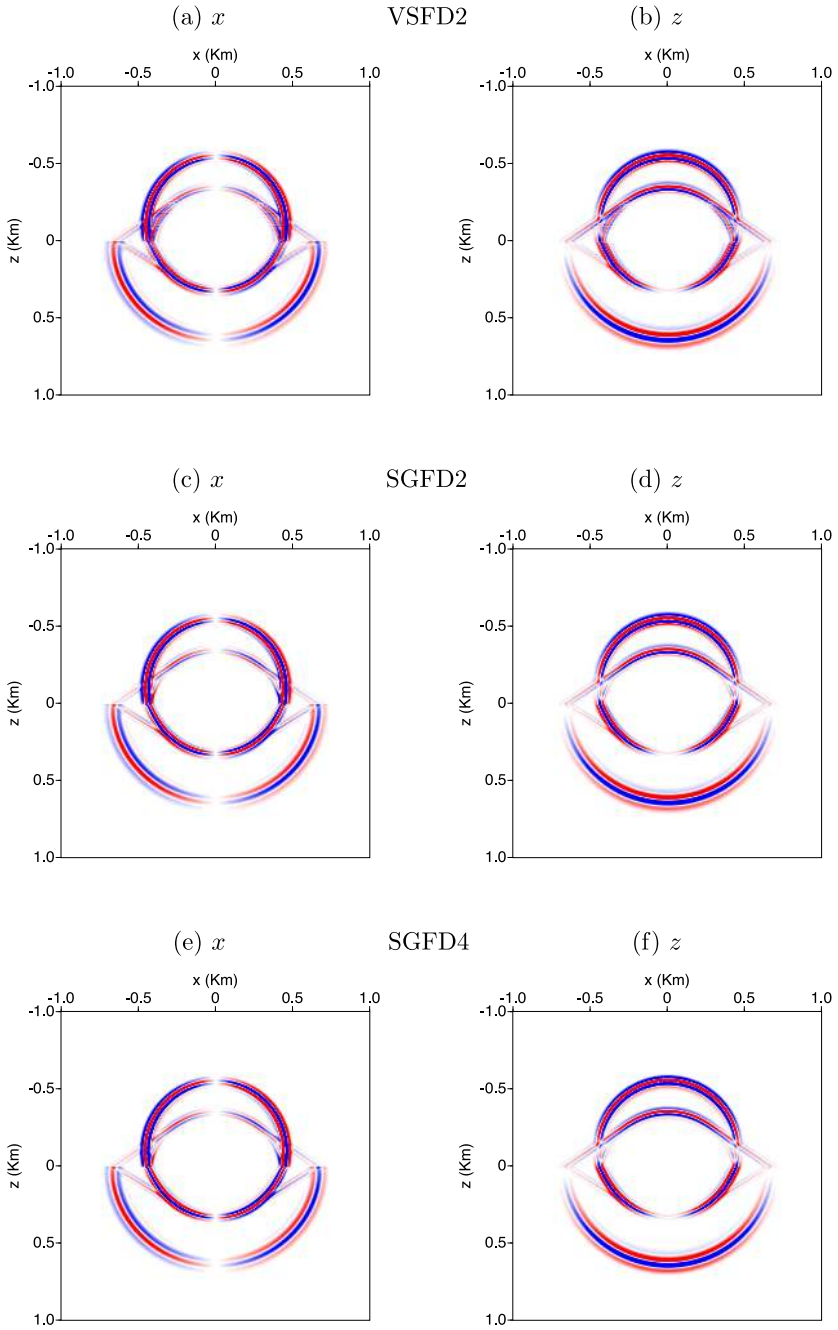

Figure 4. Snapshots of the displacement field at $t = 0.4$ s of the first numerical experiment. (a,b) VSFD2 using $h = 1.25$ m, (c,d) SGFD2 using $h = 2.5$ m, and (e,f) SGFD4 using $h = 2.5$ m.

advantage is that this formulation can naturally accommodate any type of boundary condition.

3 NUMERICAL METHODS

3.1 Finite-difference methods

There are many possible ways to discretize the wave equation using the FDM; for example, the classical standard-grid displacement formulation (Kelly *et al.* 1976), the staggered-grid velocity-stress formulation (Virieux 1984, 1986), the rotated staggered-grid formulation (Saenger *et al.* 2000), the standard-grid velocity-stress formulation (VSFDM, Lombard *et al.* 2008) and the implicit staggered-grid formulation (Liu & Sen 2009). It is beyond the scope of this paper to carry out an exhaustive comparison of all these formulations. Among these, we wish to focus on VSFDM, which has attracted relatively little attention despite its simplicity and accuracy. For comparison purposes, we will also give an overview of DFDM and SGFDM, which are related to VSFDM in ways that will become evident in the following subsections.

3.1.1 Standard-grid displacement formulation

The first attempt to generate synthetic seismograms using FDM was carried out by Alterman & Karal (1968). They used the displacement formulation of the wave equation in polar coordinates

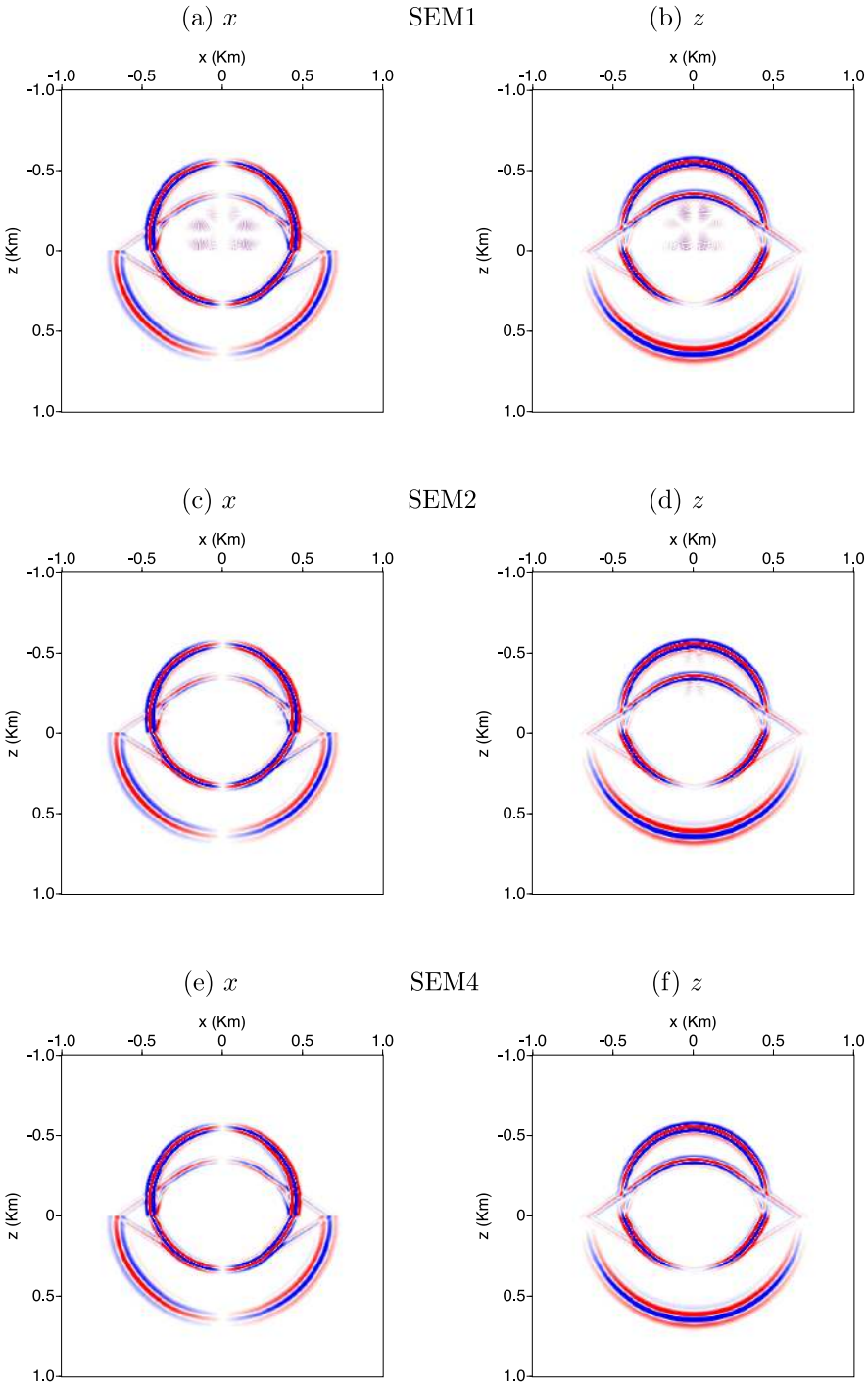

Figure 5. Snapshots of the displacement field at $t = 0.4$ s of the first numerical experiment using 37.67 nodes per wavelength and (a,b) SEM1, (c,d) SEM2 and (e,f) SEM4.

and discretized it using the classical second-order finite-difference operator. This approach was later adapted by Alford *et al.* (1974) to the acoustic wave equation and by Kelly *et al.* (1976) to the elastic wave equation. It is interesting to note that, even though the above mentioned papers present a straightforward implementation of FDM, the formulation for the elastic case is not unique because there are different ways to discretize the cross-derivative term (the second term in the right-hand side in eq. (3) for $i \neq j$; Klimeš 1996).

Since the comparison of the different methods will be based on the spatial discretization, we will only include the semidiscrete form of the equations. The discretization of the elastic wave equation by DFDM is given by (Kelly *et al.* 1976):

$$\begin{aligned}\partial_t^2 U^x_{m,n} &= \alpha^2 h^{-2}\left(U^x_{m+1,n} - 2U^x_{m,n} + U^x_{m-1,n}\right)\\ &+ \beta^2 h^{-2}\left(U^x_{m,n+1} - 2U^x_{m,n} + U^x_{m,n-1}\right)\\ &+ \frac{1}{4}h^{-2}(\alpha^2 - \beta^2)\left(U^z_{m+1,n+1} - U^z_{m+1,n-1}\right.\\ &- \left. U^z_{m-1,n+1} + U^z_{m-1,n-1}\right), \end{aligned} \tag{9}$$

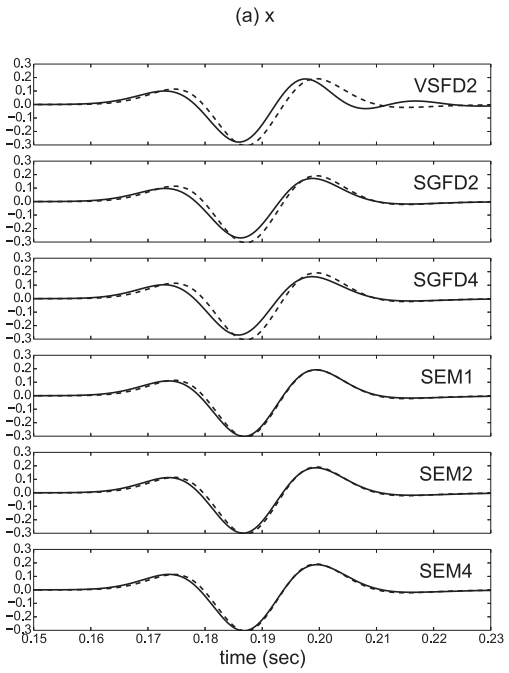

Figure 6. Comparison of the synthetic seismograms with the analytic solution (dashed line) for the first numerical experiment. The seismograms were computed 10 m above the interface at a horizontal offset of 100 m. (a) x component of displacement, (b) z component of displacement. All the seismogram plots have been created with the aid of *ObsPy* (Beyreuther *et al.* 2010; Megies *et al.* 2011).

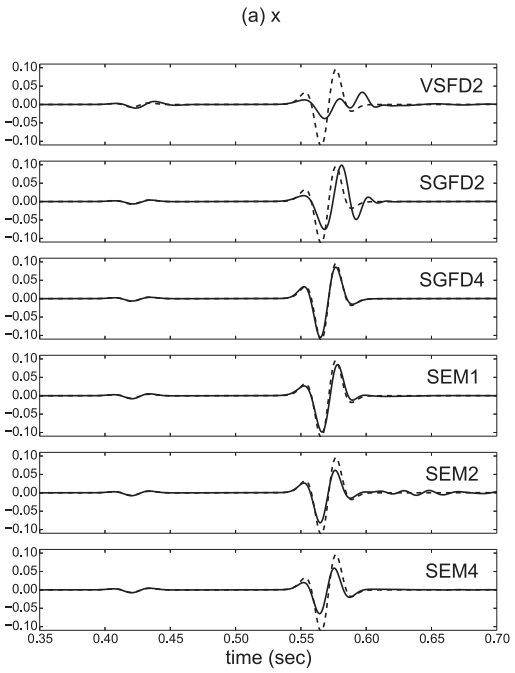

Figure 7. Synthetic seismograms for the first numerical experiment computed 10 m above the interface and at a horizontal offset of 700 m. (a) x component of displacement, (b) z component of displacement.

$$\begin{aligned}\partial_t^2 U^z_{m,n} &= \alpha^2 h^{-2}\left(U^z_{m,n+1} - 2U^z_{m,n} + U^z_{m,n-1}\right)\\ &+ \beta^2 h^{-2}\left(U^z_{m+1,n} - 2U^z_{m,n} + U^z_{m-1,n}\right)\\ &+ \frac{1}{4}h^{-2}(\alpha^2-\beta^2)\left(U^x_{m+1,n+1} - U^x_{m+1,n-1}\right.\\ &- \left. U^x_{m-1,n+1} + U^x_{m-1,n-1}\right), \end{aligned} \tag{10}$$

where h is the spatial increment in the x and z directions, $\alpha = \sqrt{(\lambda+2\mu)/\rho}$ and $\beta = \sqrt{\mu/\rho}$ are the P- and S-wave velocities, and $U^x_{m,n}$ and $U^z_{m,n}$ are the x and z components of displacement at the point (x_m, z_n).

3.1.2 *Staggered-grid velocity-stress formulation*

The SGFDM stencil takes advantage of the structure of the velocity-stress formulation to evaluate the derivatives using a centred finite-difference operator and obtain second-order accuracy in space. The

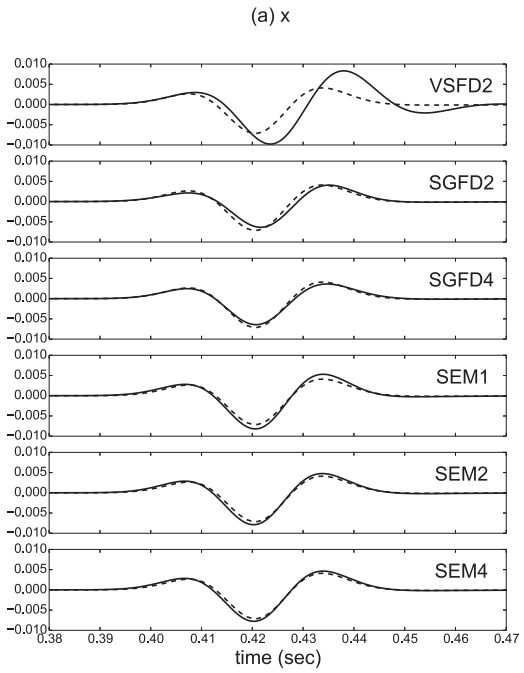

Figure 8. Details of Fig. 7(a) for the windows between 0.38 and 0.47 s. (a) x component of displacement, (b) z component of displacement.

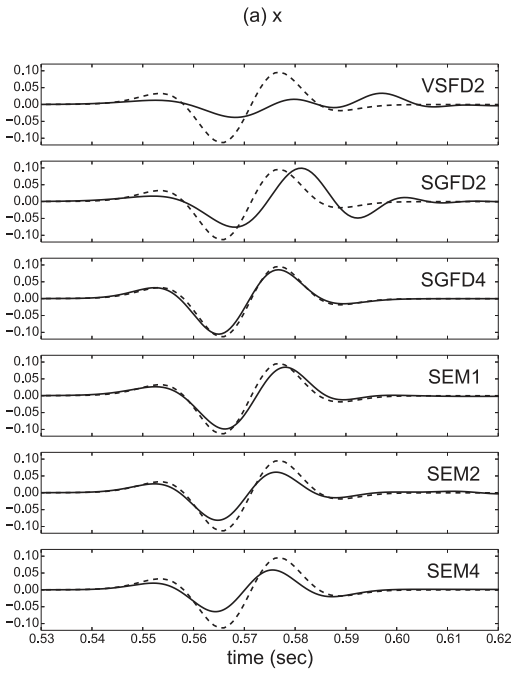

Figure 9. Details of Fig. 7(b) for the windows between 0.53 and 0.62 s. (a) x component of displacement, (b) z component of displacement.

method was originally developed by Yee (1966) for Maxwell's equations and then used in seismic modelling by Madariaga (1976). This method was successfully applied to elastic wave propagation by Virieux (1984, 1986) and has been extended to higher-order approximations in Levander (1988) and to 3-D in Graves (1996) and Minkoff (2002). See also Dougherty & Stephen (1991) and Stephen (1996) for an application of this method to sea-surface scattering in 2-D and Burns & Stephen (1990) for an application to scattering in the presence of 3-D sea-surface topography.

The semidiscrete version of the staggered-grid equations is given by (Virieux 1986)

$$\partial_t V^x_{m+1/2,n} = \frac{\bar{b}_{m+1/2,n}}{h}\left(T^{xx}_{m+1,n} - T^{xx}_{m,n} + T^{xz}_{m+1/2,n+1/2} - T^{xz}_{m+1/2,n-1/2}\right), \tag{11}$$

$$\partial_t V^z_{m,n+1/2} = \frac{\bar{b}_{m,n+1/2}}{h}\left(T^{xz}_{m+1/2,n+1/2} - T^{xz}_{m-1/2,n+1/2} + T^{zz}_{m,n+1} - T^{zz}_{m,n}\right), \tag{12}$$

$$\partial_t T^{xx}_{m,n} = \frac{\lambda_{m,n} + 2\mu_{m,n}}{h}\left(V^x_{m+1/2,n} - V^x_{m-1/2,n}\right)$$

Table 1. Misfits of the synthetic seismograms in Fig. 6 of the first numerical experiment computed using the continuous wavelet transform.

	x		z	
Method	EM	PM	EM	PM
VSFD2	0.160	0.173	0.076	0.123
SGFD2	0.108	0.125	0.095	0.133
SGFD4	0.120	0.138	0.113	0.153
SEM1	0.078	0.086	0.107	0.074
SEM2	0.070	0.090	0.089	0.084
SEM4	0.081	0.081	0.094	0.081

Table 2. Misfits of the synthetic seismograms in Fig. 7 of the first numerical experiment.

	x		z	
Method	EM	PM	EM	PM
VSFD2	0.684	0.262	0.164	0.099
SGFD2	0.216	0.155	0.174	0.092
SGFD4	0.088	0.095	0.120	0.137
SEM1	0.146	0.027	0.092	0.054
SEM2	0.309	0.119	0.081	0.092
SEM4	0.423	0.175	0.088	0.080

$$+\frac{\lambda_{m,n}}{h}\left(V^z_{m,n+1/2}-V^z_{m,n-1/2}\right), \tag{13}$$

$$\partial_t T^{zz}_{m,n}=\frac{\lambda_{m,n}}{h}\left(V^x_{m+1/2,n}-V^x_{m-1/2,n}\right)+\frac{\lambda_{m,n}+2\mu_{m,n}}{h}\left(V^z_{m,n+1/2}-V^z_{m,n-1/2}\right), \tag{14}$$

$$\partial_t T^{xz}_{m+1/2,n+1/2}=\frac{\bar{\mu}_{m+1/2,n+1/2}}{h}\left(V^x_{m+1/2,n+1}-V^x_{m+1/2,n}+V^z_{m+1,n+1/2}-V^z_{m,n+1/2}\right), \tag{15}$$

where $V^x_{m,n}$ and $V^z_{m,n}$ are the x and z components of the velocity field, and $T^{xx}_{m,n}$, $T^{zz}_{m,n}$ and $T^{xz}_{m,n}$ are the components of the stress tensor, $\bar{b}_{m+1/2,n}$ is the average buoyancy between nodes (m, n) and $(m+1, n)$, $\bar{b}_{m,n+1/2}$ is the average buoyancy between nodes (m, n) and $(m, n+1)$, and $\bar{\mu}_{m+1/2,n+1/2}$ is the average of μ at the centre of the cell defined by the nodes (m, n), $(m+1, n)$, $(m, n+1)$ and $(m+1, n+1)$. Notice that eqs (11), (12) and (15) require to evaluate the medium parameters at intermediate points between nodes, see van Vossen *et al.* (2002), Mittet (2002) and references there in for some proposed averaging strategies. The averaging adopted in this paper is the one adopted by Graves (1996), which is given by

$$\bar{b}_{m,n+1/2}=\frac{1}{2}\left(\rho^{-1}_{m,n}+\rho^{-1}_{m,n+1}\right), \tag{16}$$

$$\bar{b}_{m,n+1/2}=\frac{1}{2}\left(\rho^{-1}_{m,n}+\rho^{-1}_{m+1,n}\right), \tag{17}$$

$$\bar{\mu}_{m+1/2,n+1/2}=4\left(\mu^{-1}_{m,n}+\mu^{-1}_{m+1,n}+\mu^{-1}_{m,n+1}+\mu^{-1}_{m+1,n+1}\right)^{-1}. \tag{18}$$

The discretization in time is usually also implemented in a staggered fashion such that the method is second-order accurate in the time domain. The above equations can be easily modified for higher-order differentiation, see for example Levander (1988) and Mittet (2002). One of the advantages of this approach is that it effectively doubles the sampling ratio because of the staggering (Carcione *et al.* 2002). Another advantage is that the grid dispersion is significantly improved with respect to DFDM (this property will be reviewed in the next section). The disadvantages are that the number of degrees of freedom is larger than that of DFDM and that it is impossible to match the medium discontinuities with a staggered grid, even for simple models with straight interfaces, and therefore the error associated with the misalignment is unavoidable (Symes & Vdovina 2009). Furthermore, Lombard *et al.* (2008) summarized the difficulties and accuracy limitations of imposing free-surface boundary conditions and proposed an alternative strategy that is incompatible with a staggered grid.

3.1.3 Standard-grid velocity-stress formulation

The above equations for SGFDM can also be adapted in a standard grid using second-order operators as follows:

$$\partial_t V^x_{m,n}=\frac{1}{2h\rho}\left(T^{xx}_{m+1,n}-T^{xx}_{m-1,n}+T^{xz}_{m,n+1}-T^{xz}_{m,n-1}\right), \tag{19}$$

$$\partial_t V^z_{m,n}=\frac{1}{2h\rho}\left(T^{xz}_{m+1,n}-T^{xz}_{m-1,n}+T^{zz}_{m,n+1}-T^{zz}_{m,n-1}\right), \tag{20}$$

$$\partial_t T^{xx}_{m,n}=\frac{\lambda+2\mu}{2h}\left(V^x_{m+1,n}-V^x_{m-1,n}\right) \tag{21}$$

$$+\frac{\lambda}{h}\left(V^z_{m,n+1}-V^z_{m,n-1}\right), \tag{22}$$

$$\partial_t T^{zz}_{m,n}=\frac{\lambda}{2h}\left(V^x_{m+1,n}-V^x_{m-1,n}\right) \tag{23}$$

$$+\frac{\lambda+2\mu}{h}\left(V^z_{m,n+1}-V^z_{m,n-1}\right), \tag{24}$$

$$\partial_t T^{xz}_{m,n}=\frac{\mu}{2h}\left(V^x_{m,n+1}-V^x_{m,n-1}+V^z_{m+1,n}-V^z_{m-1,n}\right). \tag{25}$$

Besides the obvious simplification of the equations, there can be numerical advantages of this approach; for example, the interface error can be minimized using averaging strategies (Symes & Vdovina 2009) and the stability condition allows for times steps two times larger than in SGFDM (see Appendix C). Also, Lombard *et al.* (2008) have used this scheme coupled with the ADER method for time stepping to accurately impose free-surface boundary conditions.

3.2 Spectral-element method

SEM is a special case of FEM that uses high-order basis functions. For seismic modelling, it is usually implemented using the Gauss-Lobatto-Legendre (GLL) nodes and quadrature rules and Lagrange basis functions (Komatitsch & Vilotte 1998; Komatitsch & Tromp 1999, 2002a,b; Cohen 2002) because these yield an explicit time-marching scheme.

We can use the weak formulation of the elastic wave equation, eq. (6), to obtain a system of ODEs by introducing the finite dimensional subspace $\boldsymbol{X}_h = X_h \times X_h \subset \boldsymbol{H}^1(\Omega)$, where $X_h = \text{span}\{\phi_i\}$ and ϕ_i, $i = 1, \ldots, n$, are the polynomial basis functions. Substituting for $\boldsymbol{u}$ the approximation $\boldsymbol{u}_h \in \boldsymbol{X}_h$ given by the linear combination

$$\boldsymbol{u}_h(x,z,t)=\left(U^x_j(t)\phi_j(x,z),\ U^z_j(t)\phi_j(x,z)\right)^T, \tag{26}$$

where U^x_j and U^z_j are the coefficients of the FEM approximations to the horizontal and vertical displacement, respectively, and substituting $\boldsymbol{v}=(\phi_i,0)^T$ yields the following system of equations

$$M_{ij}\partial_{tt}U^x_j+K^1_{ij}U^x_j+K^2_{ij}U^z_j=F^x_i. \tag{27}$$

Similarly, substituting $\boldsymbol{v}=(0,\phi_i)^T$, yields

$$M_{ij}\partial_{tt}U^z_j+K^3_{ij}U^x_j+K^4_{ij}U^z_j=F^z_i, \tag{28}$$

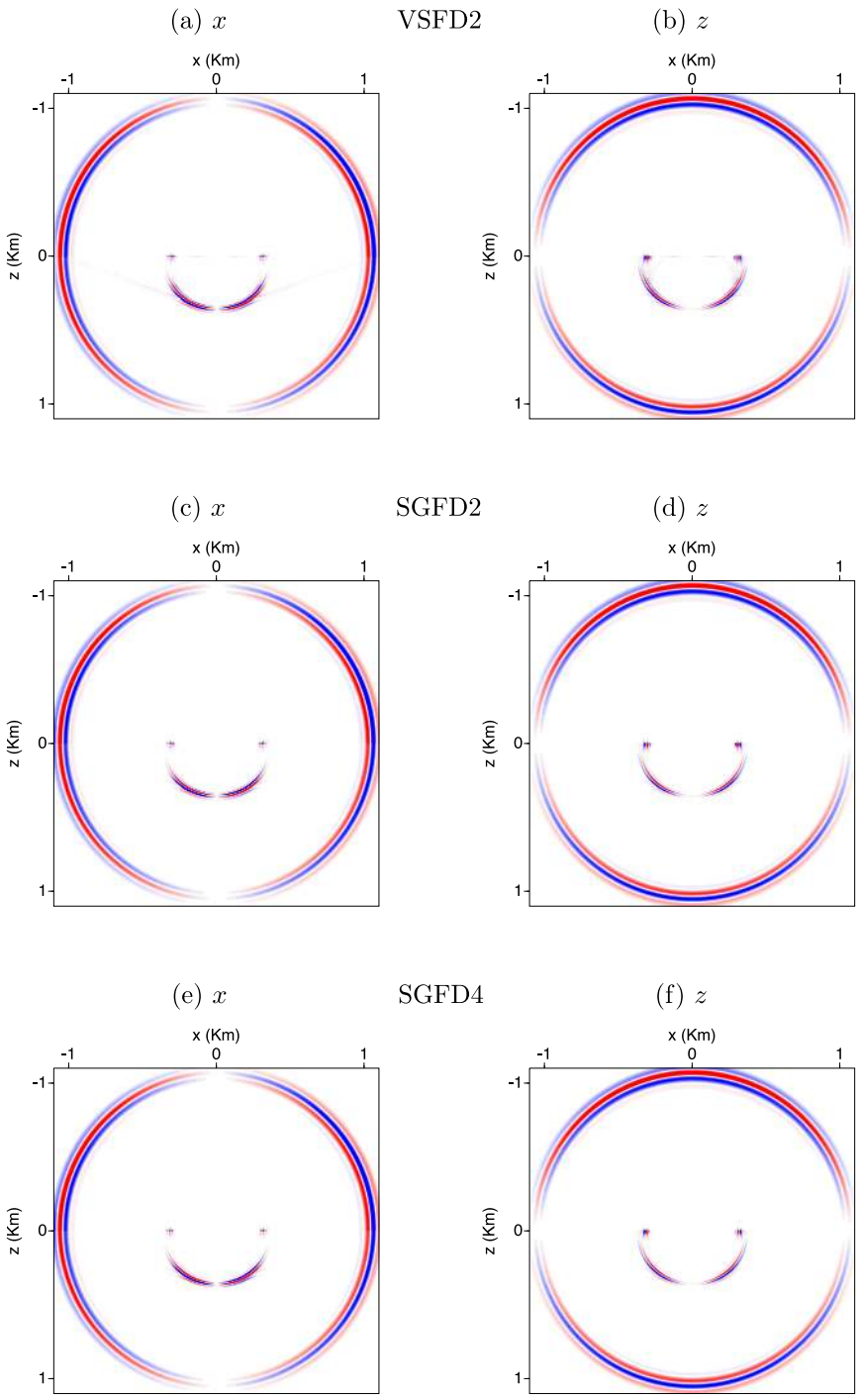

Figure 10. Snapshots of the displacement field at $t = 0.8$ s for the second numerical experiment using (a,b) VSFD2 with $h = 1$ m, (c,d) SGFD2 with $h = 2$ m, and (e,f) SGFD4 with $h = 2$ m.

where the matrices in eqs (27) and (28) are given by

$$M_{ij} = (\rho\phi_i, \phi_j)_\Omega, \tag{29}$$

$$K^1_{ij} = \boldsymbol{B}_\Omega\big((\phi_j, 0)^T, (\phi_i, 0)^T\big), \tag{30}$$

$$K^2_{ij} = \boldsymbol{B}_\Omega\big((0, \phi_j)^T, (\phi_i, 0)^T\big), \tag{31}$$

$$K^3_{ij} = \boldsymbol{B}_\Omega\big((\phi_j, 0)^T, (0, \phi_i)^T\big), \tag{32}$$

$$K^4_{ij} = \boldsymbol{B}_\Omega\big((0, \phi_j)^T, (0, \phi_i)^T\big), \tag{33}$$

$$F^x_i = (f_x, \phi_i)_\Omega, \tag{34}$$

$$F^z_i = (f_z, \phi_i)_\Omega, \tag{35}$$

and f_x and f_z are the x and z components of $\boldsymbol{f}$. Besides the advantages mentioned on eq. (6), this method has the following advantages: (i) It can minimize the discretization error by matching

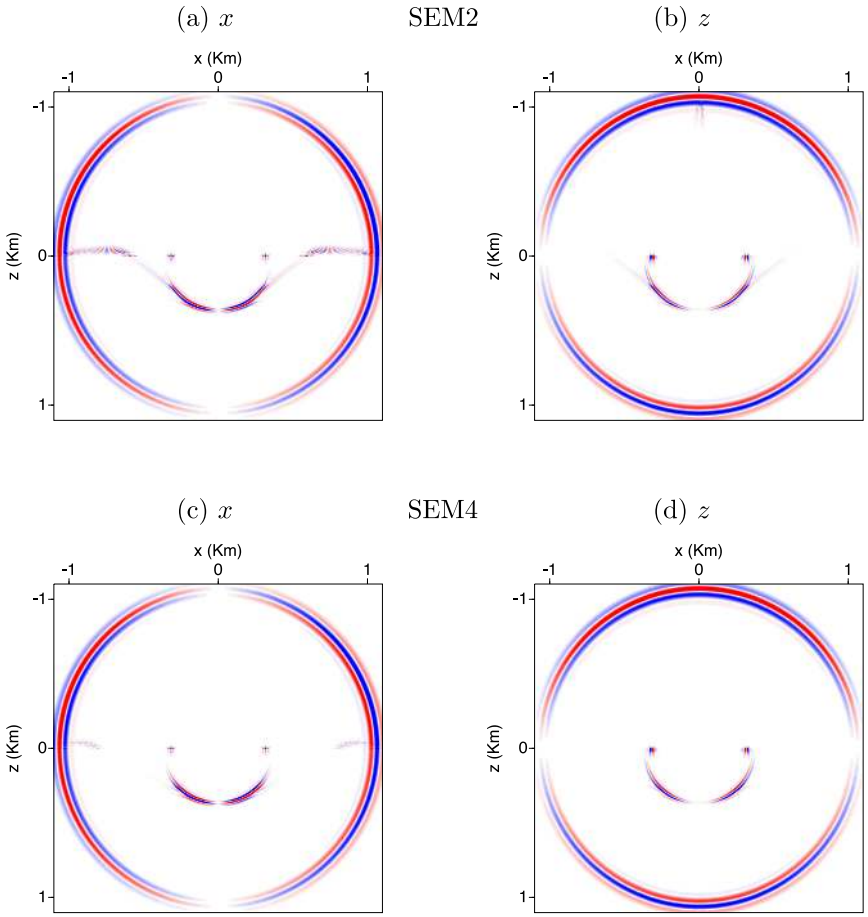

Figure 11. Snapshots of the displacement field at $t = 0.8$ s for the second numerical experiment using 34.8 nodes per wavelength and (a,b) SEM2, and (c,d) SEM4.

the medium discontinuities and topography with the finite-element mesh, and (ii) the grid-dispersion error and numerical anisotropy can be minimized by choosing a suitable polynomial order of the basis functions.

4 GRID-DISPERSION ANALYSIS

We now proceed to study the accuracy of the above mentioned methods in a domain with a fluid-solid interface. In order to do this, we study the grid dispersion of the *S*-wave in the fluid subdomain. The analyses are based on the von Neumann method (Mitchell & Griffiths 1980; Hughes 2000), which assumes a plane wave propagating through the discretized domain. Since the goal of these analyses is to derive the grid-dispersion relations, to have a manageable set of parameters we make several assumptions about the medium; we assume that the medium is isotropic, homogeneous, unbounded and source free. These are ubiquitous assumptions in plane-wave analyses, see for example Alford *et al.* (1974), Mullen & Belytschko (1982), Marfurt (1984), Cohen (2002), Ainsworth (2004a,b), Ainsworth *et al.* (2006), Zyserman *et al.* (2003), Zyserman & Gauzellino (2004, 2005), Zyserman & Santos (2007), Seriani & Oliveira (2008) and Gabriel *et al.* (2010). These assumptions are not expected to be satisfied in practice, nevertheless the results from an analysis based on these assumptions can provide valuable information to determine the discretization parameters for a numerical experiment.

4.1 Grid dispersion of the FDM

The grid dispersion of many FDMs has been analysed in the literature (e.g. Alford *et al.* 1974; Marfurt 1984; Virieux 1986; Moczo *et al.* 2000; Saenger *et al.* 2000; Cohen 2002; Liu & Sen 2009). We summarize in Appendix A the analysis for DFDM and in Appendix B the analysis of SGFDM. Also, in Appendix C we derive the grid-dispersion relations for VSFDM, which closely resemble the ones for SGFDM.

As shown in Appendix A, the *S*-wave dispersion using DFDM is given by

$$\frac{\beta_h}{\alpha} = \frac{1}{\pi\delta_s}\left(\epsilon^2\left(\sin^2(\pi\delta_s\cos\theta)+\sin^2(\pi\delta_s\sin\theta)\right)\right.$$
$$\left.+(1-\epsilon^2)\sin^2(\pi\delta_s\cos\theta)\sin^2(\pi\delta_s\sin\theta)\right)^{1/2}, \qquad (36)$$

where δ_s is the *S*-wave sampling ratio (the reciprocal of the number of nodes per wavelength), $\epsilon = \beta/\alpha$ is the *S*- to *P*-wave velocity ratio, β_h is the velocity at which the *S*-wave travels in the discretized domain and θ is the angle between the plane-wave propagation direction and the z axis. In this case, we normalize the discretized *S*-wave velocity β_h with the *P*-wave velocity, instead of the *S*-wave velocity, because we wish to consider the case with vanishing *S*-wave velocity (notice that the ratio β_h/β would converge to an undetermined value when β tends to zero). In this modified dispersion relation the absence of grid dispersion is given by $\beta_h/\alpha = \epsilon$.

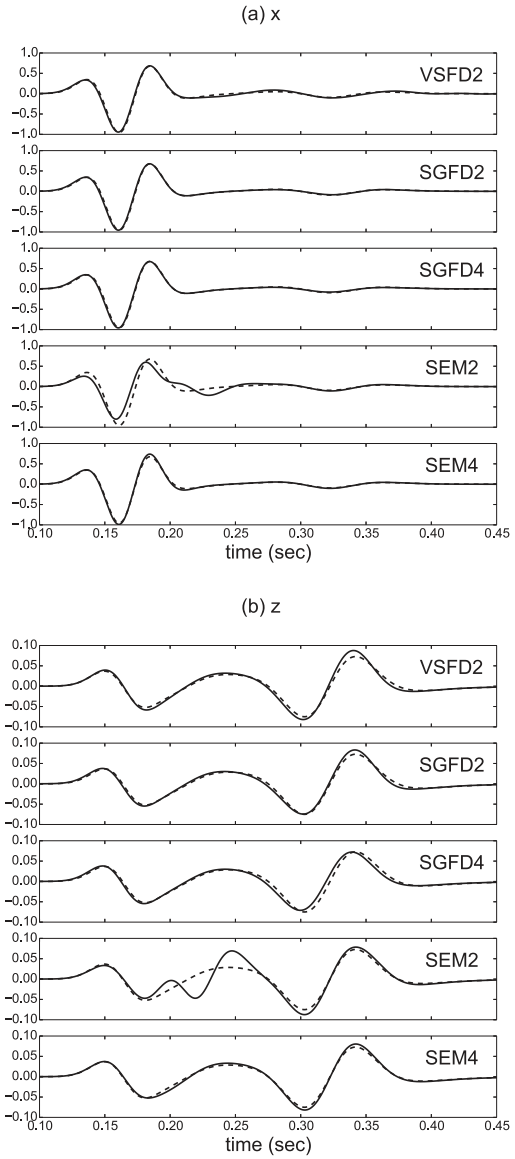

Figure 12. Synthetic seismograms for the second numerical experiment computed 10 m above the interface and at a horizontal offset of 100 m. The dashed line is the analytic solution. (a) x component of displacement, (b) z component of displacement.

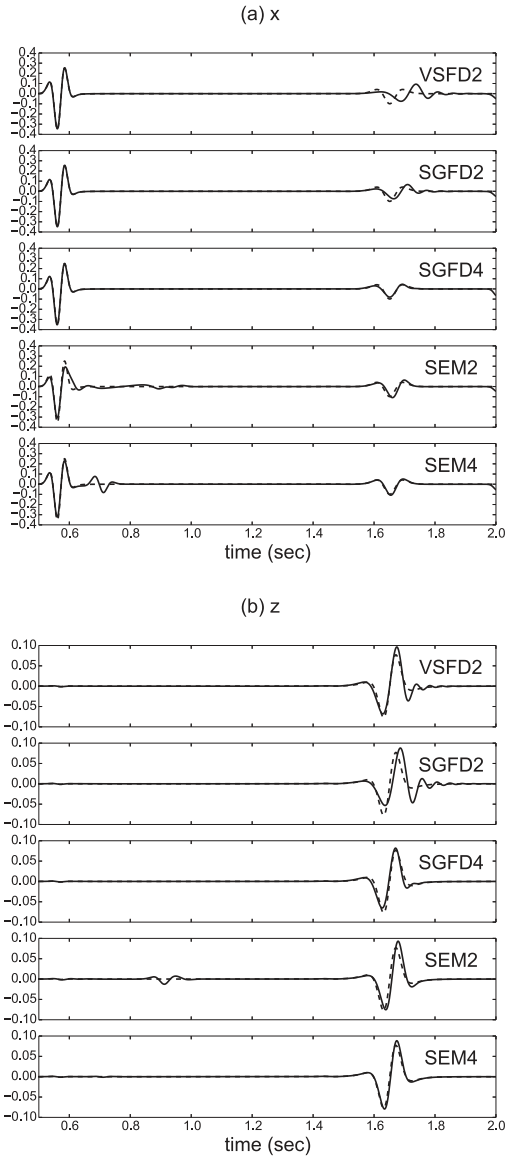

Figure 13. Synthetic seismograms for the second numerical experiment computed 10 m above the interface and at a horizontal offset of 700 m. (a) x component of displacement, (b) z component of displacement.

Setting $\epsilon = 0$ in the above equation yields

$$\frac{\beta_h}{\alpha} = \frac{1}{\pi \delta_s} |\sin(\pi \delta_s \cos\theta) \sin(\pi \delta_s \sin\theta)|, \tag{37}$$

which is not identically zero unless $\theta = 0$ or $\theta = \pi/2$, but it does converge to zero for $\delta_s \to 0$ and $\delta_s \to \infty$. Fig. 1 show the dispersion curves for different incidence angles using eq. (37); it can be observed in this figure that the maximum dispersion error is obtained at $\theta = \pi/4$.

The S-wave dispersion of SGFDM and VSFDM is given by (see Appendices B and C, respectively)

$$\text{(SGFDM)} \quad \frac{\beta_h}{\alpha} = \frac{\epsilon}{\pi \delta_s} \sqrt{\sin^2(\pi \delta_s \cos\theta) + \sin^2(\pi \delta_s \sin\theta)}, \tag{38}$$

$$\text{(VSFDM)} \quad \frac{\beta_h}{\alpha} = \frac{\epsilon}{2\pi \delta_s} \sqrt{\sin^2(2\pi \delta_s \cos\theta) + \sin^2(2\pi \delta_s \sin\theta)}. \tag{39}$$

Table 3. Misfits of the synthetic seismograms in Fig. 12 of the second numerical experiment.

	x		z	
Method	EM	PM	EM	PM
VSFD2	0.091	0.055	0.123	0.050
SGFD2	0.029	0.052	0.061	0.053
SGFD4	0.034	0.052	0.050	0.074
SEM2	0.209	0.135	0.259	0.093
SEM4	0.054	0.049	0.096	0.015

Notice that the above equations are identically zero whenever $\epsilon = 0$. Furthermore, comparing eqs (38) and (39), it is evident that in VSFDM the effective sampling ratio is double than that of SGFDM and therefore VSFDM requires the double of the nodes in each direction to yield the same accuracy as SGFDM.

In order to compare the grid dispersion of these three methods we can set a small S- to P-wave velocity ratio. Furthermore, since in practice in a medium with vanishing S-wave velocity we are

Table 4. Misfits of the synthetic seismograms in Fig. 13 of the second numerical experiment.

	x		z	
Method	EM	PM	EM	PM
VSFD2	0.216	0.221	0.171	0.080
SGFD2	0.098	0.084	0.234	0.154
SGFD4	0.065	0.052	0.055	0.101
SEM2	0.296	0.069	0.170	0.094
SEM4	0.222	0.081	0.091	0.028

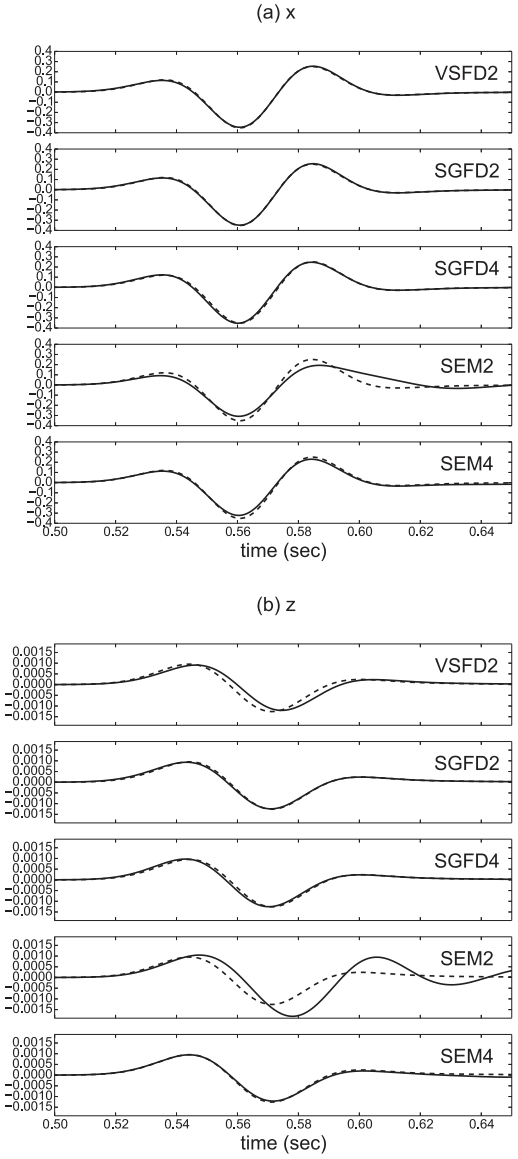

Figure 14. Details of Fig. 13 for the time window between 0.5 and 0.65 s. (a) x component of displacement, (b) z component of displacement.

interested in the *P*-wave, we assume that the sampling ratio is set according to the *P*-wave velocity therefore the *S*-wave is under sampled and δ_s is large. Fig. 2 shows the grid-dispersion curves for DFDM, SGFDM and VSFDM using $\epsilon = 0.01$. This figure shows that the dispersion of SGFDM and VSFDM is smaller than ϵ, but that of DFDM is approximately 50 times larger. Furthermore, the dispersion converges to 0 for a large sampling ratio, which is the case if we set the sampling ratio according to the *P*-wave velocity and the *S*-wave velocity tends to zero.

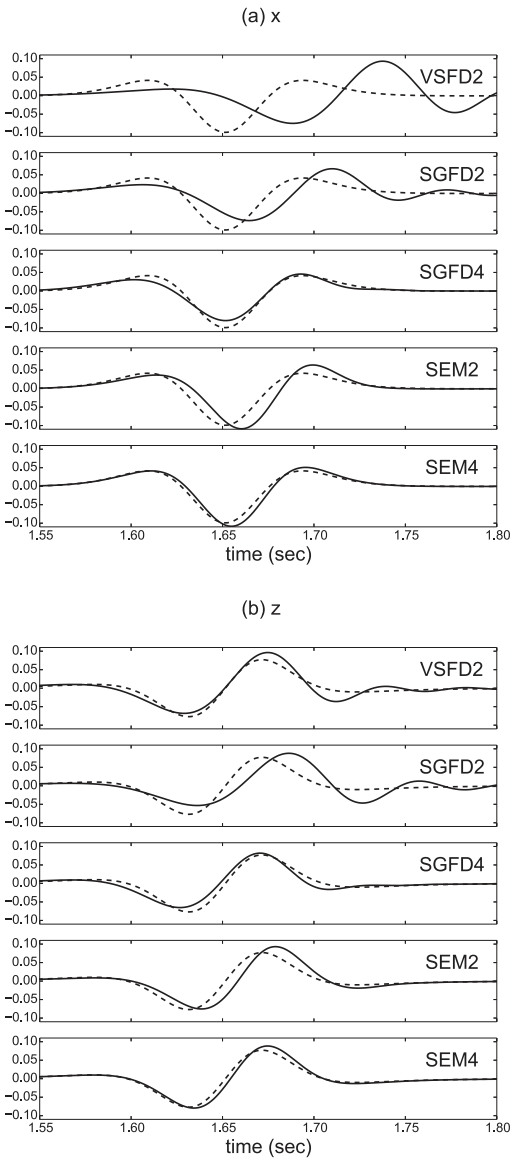

Figure 15. Details of Fig. 13 for the time window between 1.55 and 1.8 s. (a) x component of displacement, (b) z component of displacement.

4.2 Grid dispersion of the SEM

The grid dispersion of SEM for the elastic case was analysed in De Basabe & Sen (2007); the procedure is summarized in Appendix D for completeness (see also Zyserman *et al.* 2003; Seriani & Oliveira 2008, for different approaches). As mentioned in the above references, it is impractical to get explicit dispersion relations for the high-order methods, but the grid-dispersion curves can be computed numerically.

Introducing the plane-wave assumptions into the discrete system yields an eigenvalue problem of order $2\kappa^2$, where κ is the polynomial order of the method. For the first-order method there are exactly two eigenvalues, which correspond to the *P* and *S* waves, and it is possible to get explicit grid-dispersion relations. For higher values of κ it is not feasible to solve the eigenvalue problem analytically and we have to solve it numerically for each set of parameters.

The grid-dispersion relations for the first-order case are exactly those for DFDM since this method is the special case of SEM for $\kappa = 1$ and quadrilateral elements with sides parallel to the

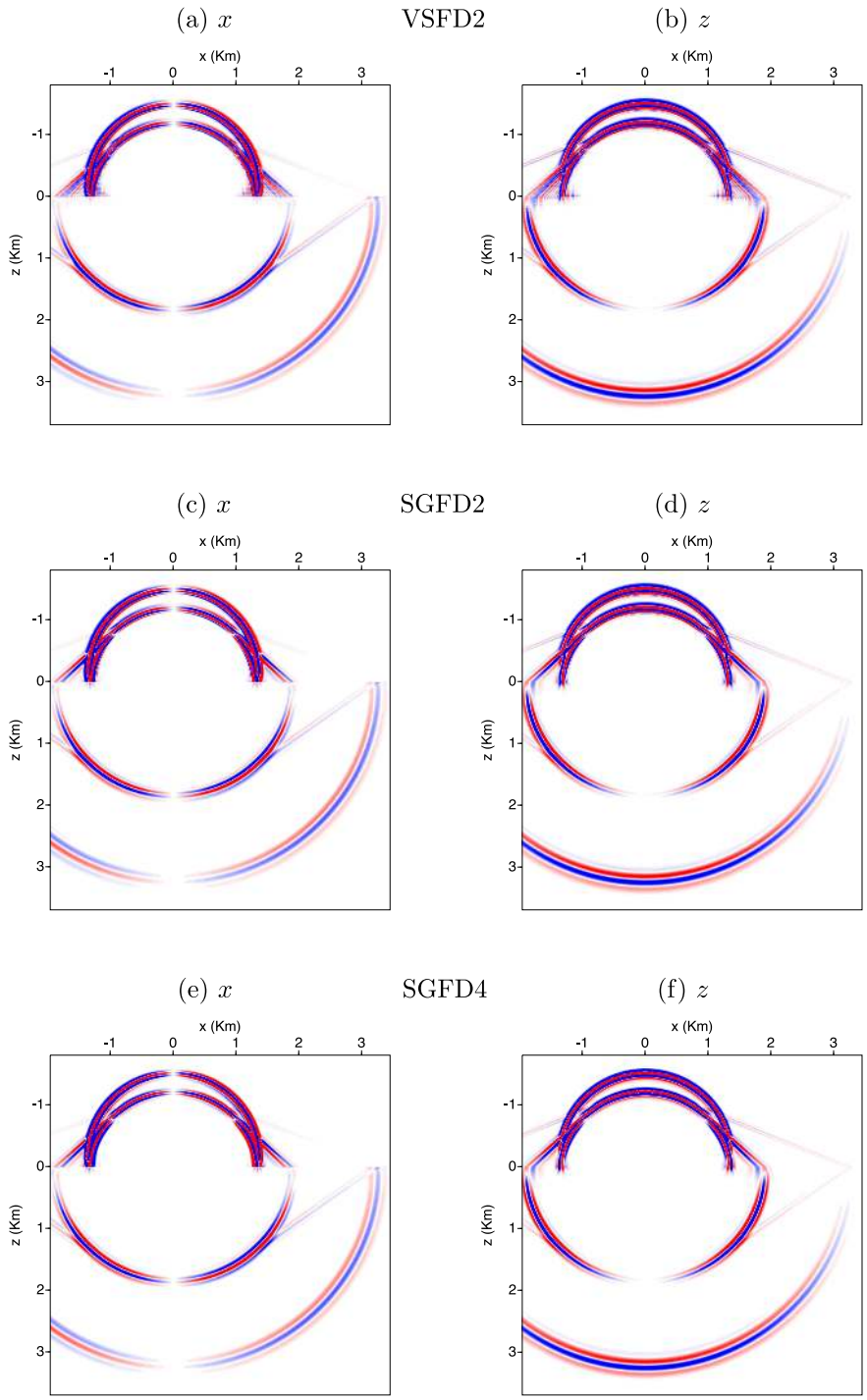

Figure 16. Snapshots of the displacement field at $t = 1$ s of the third numerical experiment using (a,b) VSFD2 with $h = 2.5$ m, (c,d) SGFD2 with $h = 5$ m and (e,f) SGFD4 with $h = 5$ m.

coordinate axes. For the same reason, the first-order SEM suffers from the catastrophic dispersion of DFDM shown in Fig. 1.

The higher-order cases have better approximation properties, as shown for example, in Cohen (2002), Ainsworth (2004a), De Basabe & Sen (2007) and Seriani & Oliveira (2008). For the vanishing *S*-wave problem, the *S*-wave dispersion is identically equal to zero whenever $\kappa \geq 2$ for all incidence angles and sampling ratios, as in the SGFDM and VSFDM cases (this has been determined numerically for a large range of parameters since there are no explicit grid-dispersion relations). For comparison purposes, we can use a small value of ϵ and plot the grid-dispersion curves for different incidence angles and degrees. In Fig. 3, we show the *S*-wave dispersion for $\epsilon = 0.01$, $\kappa = 2, \ldots, 5$ and different incidence angles. The second-order method (Fig. 3a) exhibits some visible dispersion and anisotropy, with hastened wavefronts ($\beta_h/\alpha > \epsilon$) for small sampling ratios ($\delta_s < 0.5$) and delayed wavefronts ($\beta_h/\alpha < \epsilon$) for larger sampling ratios ($\delta_s > 0.7$). Comparing Figs 2(b) and 3(a), we conclude that the amount of dispersion for $\kappa = 2$ is similar to that

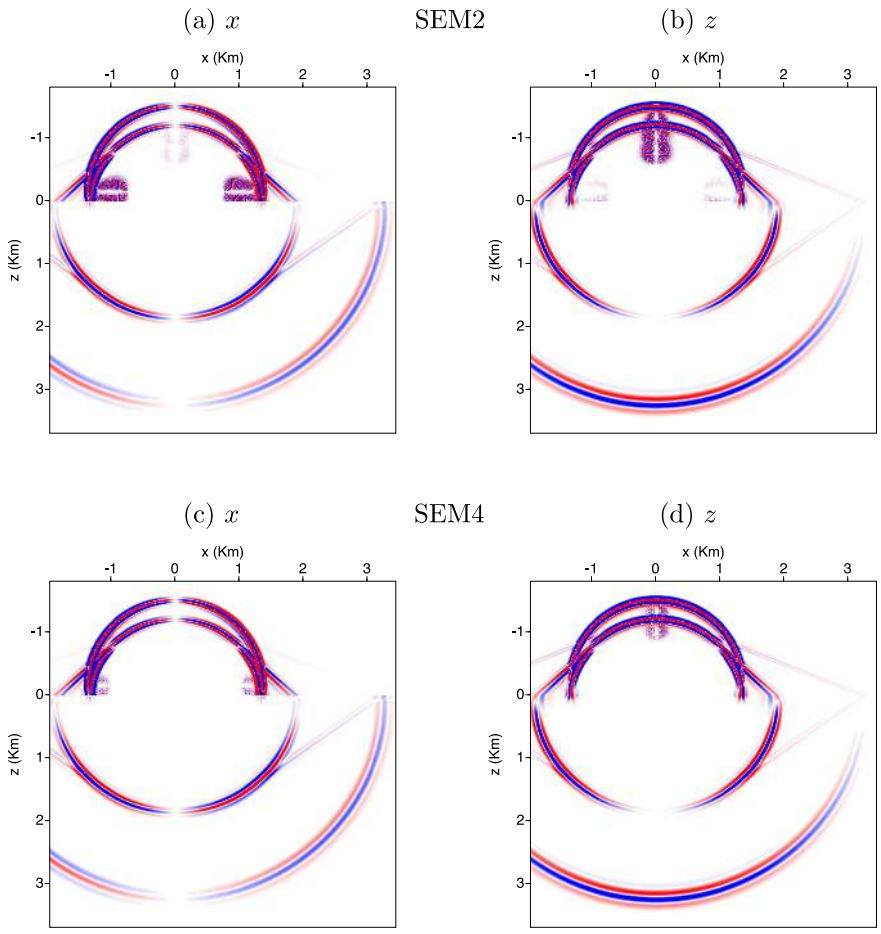

Figure 17. Snapshots of the displacement field at $t = 1$ s for the third numerical experiment using 40 nodes per wavelength and (a,b) SEM2, and (c,d) SEM4.

of SGFDM but with a different anisotropy pattern. Comparing now with Figs 3(b)–(d), for κ =3, 4 and 5, respectively, we conclude that the higher order methods yield less dispersion and anisotropy. The grid-dispersion curves for larger values of κ (not shown) exhibit a similar pattern.

5 NUMERICAL RESULTS FOR A HORIZONTAL FLUID-SOLID INTERFACE

In this section, we compare SGFDM, VSFDM and SEM using three numerical examples that include a fluid-solid interface. We will refer to the second-order VSFDM as VSFD2, and to the second- and fourth-order SGFDM as SGFD2 and SGFD4, also SEMκ will refer to SEM using basis functions of κth polynomial degree. In the following discussion, the reported sampling ratios are based on the wavelength of the *S*-wave at the peak frequency for convenience. Notice that shorter wavelengths are also present in the model because the source wavelength contains a range of frequencies and also the interface waves travel at a velocity smaller than that of the *S*-wave. Furthermore, all the considered methods are coupled with a second-order leap-frog scheme for the discretizations in time. The size of the time step is selected using the CFL stability conditions since using a smaller time step does not guarantee more accurate results (Alford *et al.* 1974; Moczo *et al.* 2000; De Basabe & Sen 2010). The numerical error of the time-stepping scheme is not negligible but it is assumed to equally affect all the considered methods.

5.1 First numerical experiment

The model for the first numerical example is divided into two horizontal layers, the top layer represents a fluid with $\alpha = 1.5$ km s^{-1} and $\rho = 1$ g cm^{-3}, and the bottom one represents a solid with $\alpha = 2.7$ km s^{-1}, $\beta = 1.4$ km s^{-1} and $\rho = 1.2$ g cm^{-3} (taken from Zhu & Popovics 2006). There is an explosive source in the pressure field located in the fluid layer 0.1 km above the interface at the point (0 km, -0.1 km). The source wavelet is the second derivative of a Gaussian function (a Ricker wavelet) with a peak frequency of 30 Hz. The snapshots at $t = 0.4$ s are shown in Figs 4 and 5. Figs 4(a) and (b) show the snapshots of the x and z components of displacement using VSFD2 and 37.67 nodes per wavelength ($h = 1.25$ m), and Figs 4(c) to (f) corresponds to SGFD2 and SGFD4 using $h = 2.5$ m for an effective sampling ratio of $\delta_s = 1/37.67$ (37.67 nodes per wavelength). The only small difference among the VSFD2, SGFD2 and SGFD4 snapshots is that the refracted wave using VSFD2 has a slightly larger amplitude. Fig. 5 shows the snapshots of the x and z components of displacement using SEM1, SEM2 and SEM4 and 37.67 nodes per wavelength. In this figure, we observe that there is a random pattern of dispersion in the fluid layer in Figs 5(a) and (b) that corresponds to the *S*-wave dispersion, nevertheless this dispersion significantly diminishes for the second-order method (Figs 5c and d) and the fourth-order method does not

exhibit any observable dispersion in Figs 5(e) and (f), in agreement with the grid-dispersion analysis of the previous section.

In order to make a more precise comparison of the accuracy of each of the methods, we show in Figs 6 to 9 the synthetic seismograms using the above mentioned numerical methods and the exact solution computed using the Cagniard-de Hoop method. For a detailed description of this method see Cagniard (1962), chapter 6 of Aki & Richards (2002) and chapter 13 of Diaz (2005); see also Zhu & Popovics (2006) for an analytical study of the interface waves in this physical settings. We have used a source code to compute the analytic solution available from the SPICE website.[1] Fig. 6 shows the x and z components of displacement of the synthetic seismograms recorded 10 m above the interface with a horizontal offset of 100 m. Comparing the synthetic seismograms with the analytic solution reveals that SEM accurately predicts the arrival time, waveform and amplitude. Fig. 7 shows the x and z components of displacement of the synthetic seismograms recorded at the larger offset of 700 m. All the considered methods yield good approximations of the arrival times, but there are significant errors in the waveform and amplitude, particularly for the x component. We show in Figs 8 and 9 two time windows for 0.38–0.47 s and 0.53–0.62 s in order to be able to see the two main arrivals. The first arrival corresponds to the head wave associated with the transmitted P wave and the second arrival is a combination of the direct wave and the Scholte wave. All of the methods except VSFD2 simulate with good accuracy the first arrival, but for the second arrival (Fig. 9) some of the methods fail to reproduce the waveform. In particular for the x component, notice in Fig. 9(a) that VSFD2 approximates poorly the waveform, and SEM2 and SEM4 underestimate the amplitude. Also, notice in Fig. 9(b) that VSFD2 and SGFD2 exhibit some dispersion. In order to make a precise comparison, we have estimated the misfit of the synthetic seismograms using an approach based on the continuous wavelet transform as proposed in Kristeková *et al.* (2006) and further developed in Kristeková *et al.* (2009). This approach allows us to separately evaluate phase and amplitude errors and it is therefore more adequate for time-series comparisons; it yields two single-valued measures of error, the envelope misfit (EM) quantifies amplitude errors and the phase misfit (PM) quantifies errors related to time or phase shifting. In order to make a qualitative evaluation of these error measures, they have proposed ranges of these values and categorized them as excellent, good, fair and poor, see fig. 1 in Kristeková *et al.* (2009). EM and PM of the simulated seismograms are shown in Tables 1 and 2. Notice that, at the short offset (Table 1), all the methods yield excellent results according to the verbal value of the goodness of fit criteria of Kristeková *et al.* (2009), however VSFD2 yields the largest misfits for the x component and SGFD4 yields the largest misfits for the z component. Furthermore, SEM yields overall low misfits for the x and z components, nevertheless SEM1 has large dispersion errors that are not reflected in the computed misfits because the dispersed waves are very slow and are not visible in the seismograms, but are clearly present in the snapshots of Figs 5(a) and (b). Having shown analytically and numerically that SEM1 produces a spurious S-wave in the fluid, we will not consider this method in the other numerical simulations. Table 2 shows the misfits of the seismograms for the larger offset. It can be observed in this table that SEM yields excellent approximations for the z component but the amplitude of the x component is approximated poorly by the high-order methods. Overall, SGFD4 yields the best approximations at the large offset except that the phase misfit of the z component is comparatively large.

[1] Seismic Wave Propagation and Imaging in Complex media: an European network (SPICE). http://www.spice-rtn.org.

5.2 Second numerical experiment

In the second numerical example, we replaced the medium parameters of the elastic layer with $\alpha = 1.5$ km s^{-1}, $\beta = 0.522$ km s^{-1} and $\rho = 1.6$ gr cm^{-3} to represent a soft sediment (modified from Carcione & Helle 2004). For this numerical experiment the source is placed 0.01 km above the interface and has a peak frequency of 15 Hz. Figs 10 and 11 show the snapshots at 0.8 s for the x and z components of displacement, all of the methods use 34.8 nodes per wavelength for the peak frequency of the S wave. Notice in all the snapshots that since the source is very close to the interface, the direct and reflected waves are indistinguishable. Furthermore, wavefronts of the transmitted P and S waves are clearly visible in the solid layer. The head wave is clearly visible in the VSFD2 snapshots but it has a very small amplitude in all the other snapshots. In addition to that, all the methods show in the snapshots a surface wave that propagates at a velocity slightly slower than that of the S wave, this is identified as the Scholte wave in Zhu & Popovics (2006) or as the Stoneley wave in Carcione & Helle (2004). Finally, the SEM snapshots (Fig. 11) show a spurious surface wave that propagates at a velocity smaller than that of the P wave but larger than that of the S wave. This spurious mode has a larger amplitude in the x component, it has a slower velocity in SEM2 than in SEM4 and generates a head wave in the solid layer and a dispersed wave in the fluid layer.

The synthetic seismograms for this experiment are shown in Figs 12 and 13. The seismograms in Fig. 12 are taken 10 m above the interface at a horizontal offset of 100 m and the corresponding envelope and phase misfits are shown in Table 3. Notice in the seismograms and in the misfits that all the methods except SEM2 accurately simulate the waveform and amplitudes of the x and z components. Translating the misfits to verbal values, all the results are in the excellent range except for those of SEM2, which can be qualified as good (see fig. 1 of Kristeková *et al.* 2009). We show also the seismograms taken at an offset of 700 m in Fig. 13 and the respective misfits in Table 4. The spurious surface wave is clearly visible in the SEM2 and SEM4 seismograms and this is reflected in the large values of EM for the x component of SEM2 and SEM4. Figs 14 and 15 show the same seismograms but focusing on the 0.5–0.65 s and 1.55–1.8 s time windows. Notice in Fig. 14 that all the methods were able to accurately simulate the direct arrival except SEM2 because of the contamination by the spurious surface wave. The second arrival is dominated by the Scholte wave and it is shown in Fig. 15. In this figure it is evident that VSFD2 and SGFD2 fail to simulate the waveform, specially for the x component. Comparing the misfits of each of the methods in Table 4, SGFD4 yields overall the most accurate results and SEM4, despite the spurious surface wave, has an excellent accuracy except for the amplitude of the x component.

5.3 Third numerical experiment

Finally, we considered a third numerical example in which we used the following parameters for the elastic layer: $\alpha = 4$ km s^{-1}, $\beta = 2.3$ km s^{-1} and $\rho = 2.4$ gr cm^{-3} (Zhu & Popovics 2006). The source has a peak frequency of 15 Hz and is placed 150 m above the interface to enhance the amplitude of the leaky Rayleigh mode

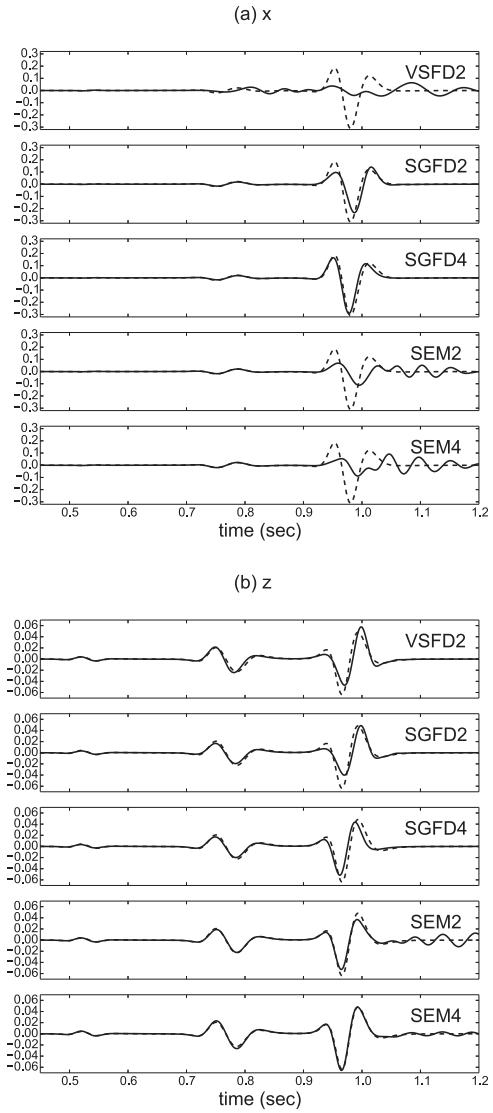

Figure 18. Comparison of the synthetic seismograms with the analytic solution (dashed line) for the third numerical experiment. The seismograms were computed 10 m above the interface and at a horizontal offset of 1.3 km from the source. (a) x component displacement, (b) z component displacement.

(Zhu & Popovics 2006). For this numerical experiment we use 40 nodes per wavelength for all the numerical methods.

The displacement field computed using the various methods at $t = 1$ s are shown in Figs 16 and 17. These snapshots are heavily clipped for visualization purposes, in order to better appreciate the head waves. There is significant dispersion at the interface in the VSFD2 snapshots, Figs 16(a) and (b). Also, there is dispersion in the fluid layer in the SEM2 and SEM4 snapshots that concentrates vertically and horizontally from the source point. Fig. 18 shows the synthetic seismograms computed 10 m above the interface with a horizontal offset of 1.3 km. This figure shows that VSFD2, SEM2 and SEM4 fail to reproduce the waveform of the x component; on the other hand, the waveform of the z component is simulated by all the methods. Notice in Table 5 that SGFD4 produces the best approximation to the x component but SEM4 yields the most accurate results for the z component. Similar conclusions can be drawn from the seismograms computed at a horizontal offset of 2.1 km, see Fig. 19 and Table 6. Notice from the table that VSFD2, SEM2 and SEM4 yield poor values for the x component. Fig. 20 shows a

Table 5. Misfits of the synthetic seismograms in Fig. 18 of the third numerical experiment.

	x		z	
Method	EM	PM	EM	PM
VSFD2	0.761	0.407	0.138	0.090
SGFD2	0.245	0.098	0.220	0.076
SGFD4	0.136	0.117	0.195	0.148
SEM2	0.672	0.313	0.402	0.060
SEM4	0.685	0.397	0.092	0.046

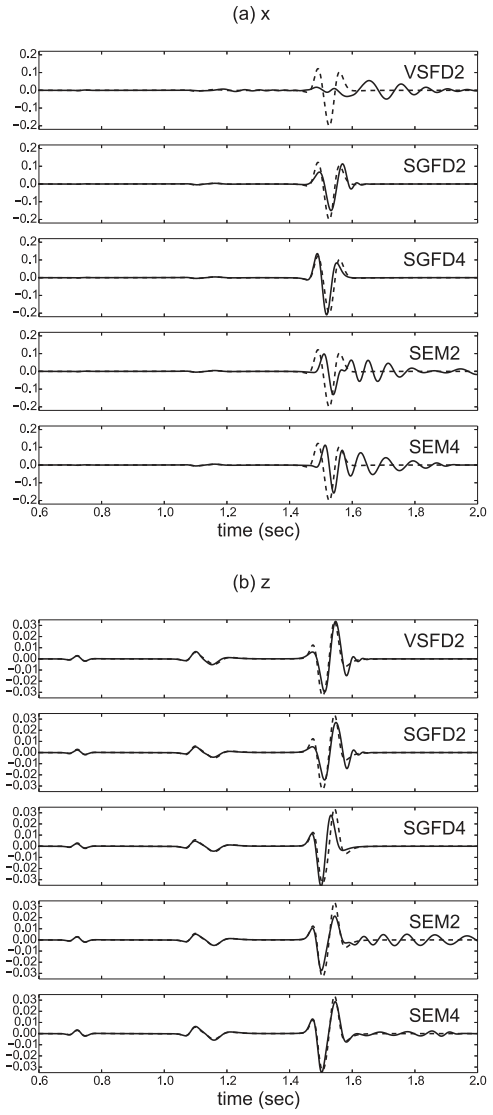

Figure 19. Comparison of the synthetic seismograms with the analytic solution for the third numerical experiment. The seismograms were computed 10 m above the interface and at a horizontal offset of 2.1 km from the source. (a) x component displacement, (b) z component displacement.

time window between 0.65 and 1.3 s in order to better appreciate the waveform of the first two arrivals in Fig. 19. The first arrival corresponds to the head wave associated to the transmitted P wave, and the second one is a combination of the head wave associated to the transmitted S wave and the leaky Rayleigh wave. These arrivals are accurately simulated by all the methods, except that the x component of the VSFD2 seismogram shows significant dispersion in the second arrival. Fig. 21 shows a time window between 1.4

Table 6. Misfits of the synthetic seismograms in Fig. 19 of the third numerical experiment.

	x		*z*	
Method	EM	PM	EM	PM
VSFD2	0.811	0.500	0.121	0.070
SGFD2	0.241	0.112	0.218	0.078
SGFD4	0.181	0.174	0.219	0.205
SEM2	0.504	0.407	0.351	0.083
SEM4	0.571	0.436	0.132	0.057

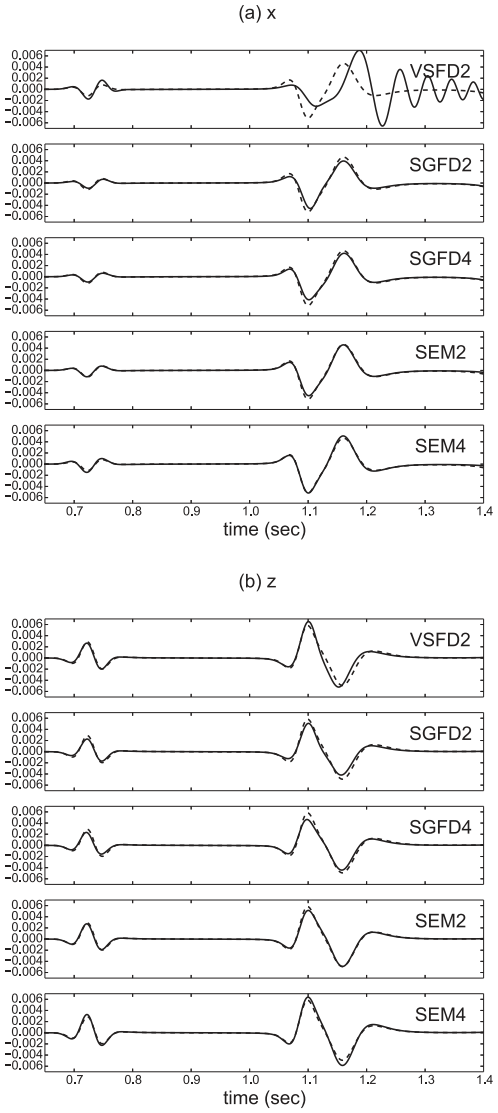

Figure 20. Details of Fig. 19 for the time window between 0.65 and 1.3 s. (a) *x* component of displacement, (b) *z* component of displacement.

and 1.7 s in order to better appreciate the waveform of the third arrival, which is a combination of the direct wave, reflected wave and Scholte wave. We observe from Fig. 21(a) that only SGFD4 can simulate the *x* component of this arrival with good accuracy. The *z* component, Fig. 21(b), is simulated by all the methods but with various degrees of accuracy: the SGFD4 waveform does not have any visible dispersion but has the largest phase error; on the other hand, SEM4 accurately reproduces the waveform but introduces a small amount of dispersion after the wavefront.

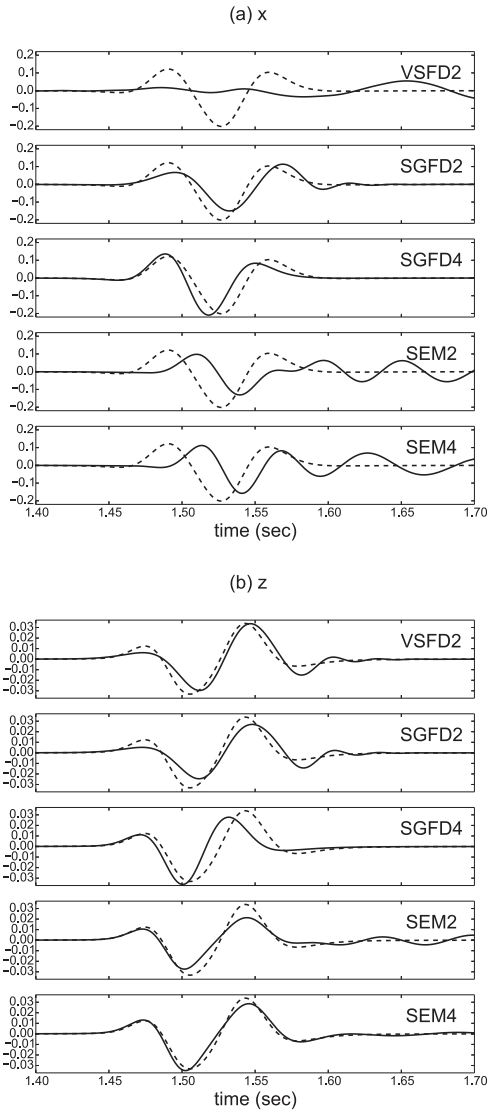

Figure 21. Details of Fig. 19 for the time window between 1.4 and 1.7 s. (a) *x* component of displacement, (b) *z* component of displacement.

6 DISCUSSION

We have focused in this analysis on the monolithic methods, which are very common in practice because of their availability. Nevertheless, we emphasize that these methods offer limited accuracy, not only because the interface conditions are not incorporated into the numerical scheme, but also because an elastic formulation is used in the fluid subdomain. The analysis shows that some of the considered methods have spurious modes in the fluid subdomain that can be explained by the inadequacy of the elastic formulation in this subdomain; see for example Figs 5(a), (b), 11 and 17. In the numerical experiments that we have performed, we have not observed any spurious modes in the results obtained using the methods based on the velocity-stress formulation, their main hindrances are the simulation of the surface waves and the discretization of the interface.

It is beyond the scope of this paper to analyse other methods that circumvent the above mentioned limitations, see for example the approaches in Komatitsch *et al.* (2000), Madec *et al.* (2009) and Komatitsch (2011). In the context of FDM, see for example Dahake & Gracewski (1997). There are also the following approaches based

on the discontinuous Galerkin method: Käser & Dumbser (2008) and Wilcox *et al.* (2010).

7 CONCLUSIONS

We have compared the accuracy of DFDM, SGFDM, VSFDM and SEM in models that include a fluid-solid interface using a monolithic approach. The comparison is based on grid-dispersion analyses of each method and numerical experiments. In order to be able to make a precise comparison, we have computed synthetic seismograms using an analytic approach and calculated the envelope and phase misfits of the seismograms computed using the numerical approaches.

The grid-dispersion analysis of FDM shows that the methods based on the velocity-stress formulation of the wave equation, not necessarily with staggered grids, yield more accurate results at fluid-solid interfaces. VSFDM can yield results almost as accurate as SGFDM but requires twice as many nodes in each direction (the additional computational cost can be partially offset by taking larger time steps since the stability condition of VSFDM allows for time steps two times larger than those required by SGFDM). In contrast, DFDM exhibits significant *S*-wave dispersion even when the physical *S*-wave velocity is zero, which would produce spurious *S*-wave arrivals in the synthetic seismograms.

The analysis of SEM shows that the first-order SEM has the same dispersion as DFDM and it is therefore not suitable for wave propagation in models with fluid-solid interfaces. This phenomenon is alleviated by using higher-order basis functions, which in fact reduces the amount of dispersion error and numerical anisotropy to a minimum.

The numerical experiments confirm the analytic results and also show that the monolithic methods are able to simulate the interface waves with varying degrees of accuracy (Stephen 1991; Stephen & Swift 1994). Although the interface waves are clearly visible in the synthetic seismograms, the amplitude and phase are not accurately simulated by all the methods. We conjecture that this is a limitation of the monolithic approaches, since the specific boundary conditions are not explicitly incorporated into the numerical methods. In particular, all the considered monolithic methods struggle to accurately simulate the tangential displacement since it is assumed to be continuous in these numerical methods whereas the boundary conditions at this type of interface dictate that it should be discontinuous. Among the methods compared, VSFD2 yields the largest errors for the tangential component in most of the considered experiments. SGFD4 reproduces both components of the waveform in most of the cases with good or excellent accuracy, whereas SEM introduced a spurious surface wave in the soft-sediment model, but produced accurate results in the other considered models, in particular the 4th order method.

One limitation of the analytical comparison is that we have considered the grid dispersion of the body waves but, as shown in the numerical experiment, the interface waves are part of the physical model. Furthermore, in the analysis we consider only the mismatch of the grid velocity compared to the physical velocity, but the amplitude of the dispersed waves is not considered.

ACKNOWLEDGEMENTS

We are grateful to Luis A. Gallardo-Delgado and Pratap Sahay for their valuable observations that helped to improve the original manuscript. We would also like to acknowledge Rune Mittet and Richard Gibbson for their helpful comments. This work was partially supported by the Mexican Council of Science and Technology (CONACYT), Project 154306, and by the Programa Iberoamericano de Ciencia y Tecnología para el Desarrollo (CYTED), Project P711RT0278.

REFERENCES

Ainsworth, M., 2004a. Discrete dispersion relation for hp-version finite element approximation at high wave number, *SIAM J. Numer. Anal.,* **42**(2), 553–575.

Ainsworth, M., 2004b. Dispersive and dissipative behaviour of high order discontinuous Galerkin finite element methods, *J. Comput. Phys.,* **198**(1), 106–130.

Ainsworth, M., Monk, P. & Muniz, W., 2006. Dispersive and dissipative properties of discontinuous galerkin finite element methods for the second-order wave equation, *J. Sci. Comput.,* **27**(1), 5–40.

Aki, K. & Richards, P., 2002. *Quantitative Seismology,* 2nd edn, University Science Books.

Alford, R., Kelly, K. & Boore, D., 1974. Accuracy of finite-difference modeling of the acoustic wave equation, *Geophysics,* **39**(6), 834–842.

Alterman, Z. & Karal, F., 1968. Propagation of elastic waves in layered media by finite difference methods, *Bull. seism. Soc. Am.,* **58**(1), 367–398.

Beyreuther, M., Barsch, R., Krischer, L., Megies, T., Behr, Y. & Wassermann, J., 2010. ObsPy: a Python toolbox for seismology, *Seism. Res. Lett.,* **81**(3), 530–533.

Burns, D.R. & Stephen, R.A., 1990. Three-dimensional numerical modeling of geoacoustic scattering from seafloor topography, *J. acoust. Soc. Am.,* **88**(5), 2338–2345.

Cagniard, L., 1962. *Reflection and Refraction of Progressive Seismic Waves,* McGraw-Hill.

Carcione, J.M. & Helle, H., 2004. The physics and simulation of wave propagation at the ocean bottom, *Geophysics,* **69**(3), 825–839.

Carcione, J., Herman, G. & Ten Kroode, A., 2002. Seismic modeling, *Geophysics,* **67**(4), 1304–1325.

Cohen, G., 2002. *Higher-Order Numerical Methods for Transient Wave Equations,* Scientific Computation, Springer-Verlag.

Dahake, G. & Gracewski, S., 1997. Finite difference predictions of P-SV wave propagation inside submerged solids. I. Liquid–solid interface conditions, *J. acoust. Soc. Am.,* **102,** 2125–2137.

De Basabe, J.D. & Sen, M.K., 2007. Grid dispersion and stability criteria of some common finite-element methods for acoustic and elastic wave equations, *Geophysics,* **72**(6), T81–T95.

De Basabe, J.D. & Sen, M.K., 2010. Stability of the high-order finite elements for acoustic or elastic wave propagation with high-order time stepping, *Geophys. J. Int.,* **181**(1), 577–590.

Diaz, J., 2005. *Approches analytiques et numériques de problèmes de transmission en propagation d'ondes en régime transitoire. Application au couplage fluide-structure et aux méthodes de couches parfaitement adaptées.,* Ph.D. thesis, L'Université Paris.

Dougherty, M.E. & Stephen, R.A., 1991. Seismo/acoustic propagation through rough seafloors, *J. acoust. Soc. Am.,* **90**(5), 2637–2651.

Gabriel, D., Plešek, J., Kolman, R. & Valeš, F., 2010. Dispersion of elastic waves in the contact–impact problem of a long cylinder, *J. Comput. Appl. Math.,* **234,** 1930–1936.

Graves, R., 1996. Simulating seismic wave propagation in 3D elastic media using staggered-grid finite differences, *Bull. seism. Soc. Am.,* **86**(4), 1091–1106.

Hou, G., Wang, J. & Layton, A., 2012. Numerical methods for fluid-structure interaction – a review, *Commun. Comput. Phys.,* **12**(2), 337–377.

Hughes, T. J.R., 2000. *The Finite Element Method,* 2nd edn, Dover Publications.

Käser, M. & Dumbser, M., 2008. A highly accurate discontinuous Galerkin method for complex interfaces between solids and moving fluids, *Geophysics,* **73**(3), T23–T35.

Kelly, K., Ward, R., Treitel, S. & Alford, R., 1976. Synthetic seismograms – A finite-difference approach, *Geophysics,* **41**(1), 2–27.

Klimeš, L., 1996. Accuracy of elastic finite differences in smooth media, *Pure appl. Geophys.,* **148**(1), 39–76.
Komatitsch, D., 2011. Fluid-solid coupling on a cluster of GPU graphics cards for seismic wave propagation, *Comptes Rendus Mecanique,* **339,** 125–135.
Komatitsch, D. & Tromp, J., 1999. Introduction to the spectral element method for three-dimensional seismic wave propagation, *Geophys. J. Int.,* **139**(3), 806–822.
Komatitsch, D. & Tromp, J., 2002a. Spectral-element simulations of global seismic wave propagation-I. Validation, *Geophys. J. Int.,* **149**(2), 390–412.
Komatitsch, D. & Tromp, J., 2002b. Spectral-element simulations of global seismic wave propagation-II. Three-dimensional models, oceans, rotation and self-gravitation, *Geophys. J. Int.,* **150**(1), 303–318.
Komatitsch, D. & Vilotte, J., 1998. The spectral-element method: an efficient tool to simulate the seismic response of 2D and 3D geological structures, *Bull. seism. Soc. Am.,* **88**(2), 368–392.
Komatitsch, D., Barnes, C. & Tromp, J., 2000. Wave propagation near a fluid-solid interface: a spectral-element approach, *Geophysics,* **65**(02), 623–631.
Kristeková, M., Kristek, J., Moczo, P. & Day, S.M., 2006. Misfit criteria for quantitative comparison of seismograms, *Bull. seism. Soc. Am.,* **96**(5), 1836–1850.
Kristeková, M., Kristek, J. & Moczo, P., 2009. Time-frequency misfit and goodness-of-fit criteria for quantitative comparison of time signals, *Geophys. J. Int.,* **178**(2), 813–825.
Levander, A., 1988. Fourth-order finite-difference P-SV seismograms, *Geophysics,* **53,** 1425–1436.
Liu, Y. & Sen, M.K., 2009. An implicit staggered-grid finite-difference method for seismic modelling, *Geophys. J. Int.,* **179**(1), 459–474.
Lombard, B. & Piraux, J., 2004. Numerical treatment of two-dimensional interfaces for acoustic and elastic waves, *J. Comput. Phys.,* **195**(1), 90–116.
Lombard, B., Piraux, J., Gélis, C. & Virieux, J., 2008. Free and smooth boundaries in 2-D finite-difference schemes for transient elastic waves, *Geophys. J. Int.,* **172,** 252–261.
Madariaga, R., 1976. Dynamics of an expanding circular fault, *Bull. seism. Soc. Am.,* **66**(3), 639–666.
Madec, R., Komatitsch, D. & Diaz, J., 2009. Energy-conserving local time stepping based on high-order finite elements for seismic wave propagation across a fluid-solid interface, *Comput. Model. Eng. Sci.,* **49**(2), 163–189.
Marfurt, K.J., 1984. Accuracy of finite-difference and finite-element modeling of the scalar and elastic wave equations, *Geophysics,* **49**(5), 533–549.
Megies, T., Beyreuther, M., Barsch, R., Krischer, L. & Wassermann, J., 2011. ObsPy – what can it do for data centers and observatories? *Ann. Geophys.,* **54**(1), 47–58.
Minkoff, S., 2002. Spatial parallelism of a 3D finite difference velocity-stress elastic wave propagation codes, *SIAM J. Sci. Comput.,* **24**(1), 1–19.
Mitchell, A. & Griffiths, D., 1980. *The Finite Difference Method in Partial Differential Equations,* John Wiley and Sons.
Mittet, R., 2002. Free-surface boundary conditions for elastic staggered-grid modeling schemes, *Geophysics,* **67**(5), 1616–1623.
Moczo, P., Kristek, J. & Bystricky, E., 2000. Stability and grid dispersion of the P-SV 4th-order staggered-grid finite-difference scheme, *Studia Geophysica et Geodaetica,* **44,** 381–402.
Mullen, R. & Belytschko, T., 1982. Dispersion analysis of finite element semidiscretizations of the two-dimensional wave equation, *Int. J. Numer. Methods Eng.,* **18**(1), 11–29.
Qian, Z.-H. & Yamanaka, H., 2012. An efficient approach for simulating seismoacoustic scattering due to an irregular fluid–solid interface in multilayered media, *Geophys. J. Int.,* **189**(1), 524–540.
Saenger, E.H., Gold, N. & Shapiro, S.A., 2000. Modeling the propagation of elastic waves using a modified finite-difference grid, *Wave Motion,* **31,** 77–92.
Seriani, G. & Oliveira, S.P., 2008. Dispersion analysis of spectral element methods for elastic wave propagation, *Wave Motion,* **45**(6), 729–744.
Soares, D. Jr, 2008. Numerical modelling of acoustic–elastodynamic coupled problems by stabilized boundary element techniques, *Comput. Mech.,* **42**(6), 787–802.
Soares, D. Jr & Mansur, W.J., 2006. Dynamic analysis of fluid–soil–structure interaction problems by the boundary element method, *J. Comput. Phys.,* **219,** 498–512.
Stephen, R., 1983. A comparison of finite difference and reflectivity seismograms for marine models, *Geophys. J. R. astr. Soc.,* **72**(1), 39–57.
Stephen, R., 1991. Finite difference modelling of shear waves, in *Shear Waves in Marine Sediments,* pp. 471–478, eds Hovem, J., Richardson, M. & Stoll, R., Kluwer.
Stephen, R., 1996. Modeling sea surface scattering by the time-domain finite-difference method, *J. acoust. Soc. Am.,* **100**(4), 2070–2078.
Stephen, R.A. & Swift, S.A., 1994. Modeling seafloor geoacoustic interaction with a numerical scattering chamber, *J. acoust. Soc. Am.,* **96**(2), 973–990.
Symes, W. & Vdovina, T., 2009. Interface error analysis for numerical wave propagation, *Computat. Geosci.,* **13,** 363–371.
van Vossen, R., Robertsson, J.O.A. & Chapman, C., 2002. Finite-difference modeling of wave propagation in a fluid-solid configuration, *Geophysics,* **67**(2), 618–624.
Virieux, J., 1984. SH wave propagation in heterogeneous media: velocity-stress finite-difference method, *Geophysics,* **49**(11), 1933–1957.
Virieux, J., 1986. P-SV wave propagation in heterogeneous media: velocity-stress finite-difference method, *Geophysics,* **51**(4), 889–901.
Wilcox, L.C., Stadler, G., Burstedde, C. & Ghattas, O., 2010. A high-order discontinuous Galerkin method for wave propagation through coupled elastic-acoustic media, *J. Comput. Phys.,* **229**(24), 9373–9396.
Yee, K., 1966. Numerical solution of initial boundary value problems involving Maxwell's equations in isotropic media, *IEEE Trans. Antenn. Propag.,* **AP-14**(8), 302–307.
Zhu, J. & Popovics, J.S., 2006. Analytical study of excitation and measurement of fluid-solid interface waves, *Geophys. Res. Lett.,* **33**(9), doi:10.1029/2006GL026068.
Zyserman, F. & Gauzellino, P., 2004. Study of the numerical dispersion of FEMs for the viscoacoustic equation, *J. appl. Geophys.,* **55,** 279–289.
Zyserman, F. & Gauzellino, P., 2005. Dispersion analysis of a nonconforming finite element method for the three-dimensional scalar and elastic wave equations, *Finite Elem. Anal. Des.,* **41,** 1309–1326.
Zyserman, F. & Santos, J., 2007. Analysis of the numerical dispersion of waves in saturated poroelastic media, *Comput. Methods Appl. Mech. Eng.,* **196,** 4644–4655.
Zyserman, F., Gauzellino, P. & Santos, J., 2003. Dispersion analysis of a nonconforming finite element method for the Helmholtz and elastodynamic equations, *Int. J. Numer. Methods Eng.,* **58**(9), 1381–1395.

APPENDIX A: GRID DISPERSION ANALYSIS OF THE DISPLACEMENT FORMULATION OF FDM

The grid dispersion of the classical FDM of Kelly *et al.* (1976) has been analysed, for example, in Cohen (2002); We summarize the analysis here for completeness. Assuming a plane wave solution for the x and z components of displacement, then $U^x_{m,n} = A_1 E_{m,n}$ and $U^z_{m,n} = A_2 E_{m,n}$, where

$$E_{m,n} = \exp\{i\,(k_x mh + k_z nh - \omega_h t)\}, \tag{A1}$$

ω_h is the grid angular frequency, h is the spatial increment in the x and z directions, $(k_x, k_z)^T$ is the wavenumber, and A_1 and A_2 are arbitrary constants. Substituting the plane wave solution into eqs (9) and (10) yields the following eigenvalue problem

$$\Lambda \begin{bmatrix} A_1 \\ A_2 \end{bmatrix} = \begin{bmatrix} \Gamma & \Phi \\ \Phi & \Upsilon \end{bmatrix} \begin{bmatrix} A_1 \\ A_2 \end{bmatrix}, \tag{A2}$$

where

$$\Lambda = h^2 \omega_h^2, \tag{A3}$$

$$\Gamma = 4\alpha^2 \sin^2\left(\frac{k_x h}{2}\right) + 4\beta^2 \sin^2\left(\frac{k_z h}{2}\right), \tag{A4}$$

$$\Upsilon = 4\alpha^2 \sin^2\left(\frac{k_z h}{2}\right) + 4\beta^2 \sin^2\left(\frac{k_x h}{2}\right), \tag{A5}$$

$$\Phi = (\alpha^2 - \beta^2)\sin(k_x h)\sin(k_z h). \tag{A6}$$

The system has non-trivial solutions if $\Lambda = \Lambda_1$ or $\Lambda = \Lambda_2$, where

$$\Lambda_1 = \alpha^2\left[\sin^2\left(\frac{k_x h}{2}\right) + \sin^2\left(\frac{k_z h}{2}\right)\right] - (\alpha^2 - \beta^2)\sin^2\left(\frac{k_x h}{2}\right)\sin^2\left(\frac{k_z h}{2}\right), \tag{A7}$$

$$\Lambda_2 = \beta^2\left[\sin^2\left(\frac{k_x h}{2}\right) + \sin^2\left(\frac{k_z h}{2}\right)\right] + (\alpha^2 - \beta^2)\sin^2\left(\frac{k_x h}{2}\right)\sin^2\left(\frac{k_z h}{2}\right). \tag{A8}$$

From eqs (A3) and (A7), the grid dispersion relation of the *P*-wave is given by

$$\frac{\alpha_h}{\alpha} = \frac{1}{\pi\delta_p}\left(\sin^2(\pi\delta_p\cos\theta) + \sin^2(\pi\delta_p\sin\theta) - (1-\epsilon^2)\sin^2(\pi\delta_p\cos\theta)\sin^2(\pi\delta_p\sin\theta)\right)^{1/2}, \tag{A9}$$

and using eq. (A8), the grid dispersion of the *S* wave is given by

$$\frac{\beta_h}{\alpha} = \frac{1}{\pi\delta_s}\left(\epsilon^2\left(\sin^2(\pi\delta_s\cos\theta) + \sin^2(\pi\delta_s\sin\theta)\right) + (1-\epsilon^2)\sin^2(\pi\delta_s\cos\theta)\sin^2(\pi\delta_s\sin\theta)\right)^{1/2}, \tag{A10}$$

where $\epsilon = \beta/\alpha$ is the *S*- to *P*-wave velocity ratio, $\delta_p = h/L$ is the *P*-wave sampling ratio, $\delta_s = \delta_p/\epsilon$ is the *S*-wave sampling ratio, L is the wavelength of the *P* wave and θ is the angle between the plane-wave propagation direction and the z axis. Similar expressions using a finite-differences discretization in time were given in Cohen (2002), page 81. Note that both dispersion relations are functions of the *P*- and *S*-wave velocities.

APPENDIX B: GRID DISPERSION ANALYSIS OF THE STAGGERED-GRID FORMULATION OF FDM

The grid dispersion relations for the second- and fourth-order staggered-grid finite-difference schemes where derived in Moczo *et al.* (2000); We develop the grid-dispersion relations here for completeness. Using the plane-wave solution for the velocity and stress, then

$$U^x_{m,n} = A_1 E_{m,n}, \quad U^z_{m,n} = A_2 E_{m,n}, \tag{B1}$$

$$T^{xx}_{m,n} = B_1 E_{m,n}, \quad T^{zz}_{m,n} = B_2 E_{m,n}, \quad T^{xz}_{m,n} = B_3 E_{m,n}. \tag{B2}$$

where $E_{m,n}$ was defined in eq. (A1) and A_1, A_2, B_1, B_2 and B_3 are arbitrary constants. Substituting in the staggered-grid scheme yields

$$-h\omega_h \boldsymbol{a} = \Theta \boldsymbol{b}, \tag{B3}$$

$$-h\omega_h \boldsymbol{b} = \Psi \boldsymbol{a}, \tag{B4}$$

where $\boldsymbol{a} = (A_1,\ A_2)^T$, $\boldsymbol{b} = (B_1,\ B_2,\ B_3)^T$,

$$\Theta = \frac{2}{\rho}\begin{bmatrix} \sin\left(\frac{k_x h}{2}\right) & 0 & \sin\left(\frac{k_z h}{2}\right) \\ 0 & \sin\left(\frac{k_z h}{2}\right) & \sin\left(\frac{k_x h}{2}\right) \end{bmatrix}, \tag{B5}$$

and

$$\Psi = 2\begin{bmatrix} \rho\alpha^2 \sin\left(\frac{k_x h}{2}\right) & \lambda \sin\left(\frac{k_z h}{2}\right) \\ \lambda \sin\left(\frac{k_x h}{2}\right) & \rho\alpha^2 \sin\left(\frac{k_z h}{2}\right) \\ \rho\beta^2 \sin\left(\frac{k_z h}{2}\right) & \rho\beta^2 \sin\left(\frac{k_x h}{2}\right) \end{bmatrix}. \tag{B6}$$

Substituting eqs (B4) in (B3) yields the following 2×2 system

$$\Lambda\begin{bmatrix} A_1 \\ A_2 \end{bmatrix} = \begin{bmatrix} \Gamma & \Phi \\ \Phi & \Upsilon \end{bmatrix}\begin{bmatrix} A_1 \\ A_2 \end{bmatrix}, \tag{B7}$$

where

$$\Lambda = h^2\omega_h^2 \tag{B8}$$

$$\Gamma = 4\alpha^2 \sin^2\left(\frac{k_x h}{2}\right) + 4\beta^2 \sin^2\left(\frac{k_z h}{2}\right) \tag{B9}$$

$$\Upsilon = 4\alpha^2 \sin^2\left(\frac{k_z h}{2}\right) + 4\beta^2 \sin^2\left(\frac{k_x h}{2}\right) \tag{B10}$$

$$\Phi = 4(\alpha^2 - \beta^2)\sin\left(\frac{k_x h}{2}\right)\sin\left(\frac{k_z h}{2}\right). \tag{B11}$$

The system has non-trivial solutions if $\Lambda = \Lambda_1$ or $\Lambda = \Lambda_2$, where

$$\Lambda_1 = 4\alpha^2\left[\sin^2\left(\frac{k_x h}{2}\right) + \sin^2\left(\frac{k_z h}{2}\right)\right], \tag{B12}$$

$$\Lambda_2 = 4\beta^2\left[\sin^2\left(\frac{k_x h}{2}\right) + \sin^2\left(\frac{k_z h}{2}\right)\right]. \tag{B13}$$

The grid dispersion relation for the *P*-wave is related to Λ_1, and is given by

$$\frac{\alpha_h}{\alpha} = \frac{1}{\pi\delta_p}\sqrt{\sin^2(\pi\delta_p\cos\theta) + \sin^2(\pi\delta_p\sin\theta)}, \tag{B14}$$

and from Λ_2, the dispersion relation for the *S* wave is

$$\frac{\beta_h}{\alpha} = \frac{\epsilon}{\pi\delta_s}\sqrt{\sin^2(\pi\delta_s\cos\theta) + \sin^2(\pi\delta_s\sin\theta)}. \tag{B15}$$

APPENDIX C: GRID DISPERSION ANALYSIS OF THE STANDARD-GRID VELOCITY-STRESS FORMULATION OF FDM

In this appendix, we develop the grid-dispersion relations for the standard-grid velocity-stress formulation (VSFDM). The analysis is similar to that of SGFDM in the previous appendix. Using the plane-wave solution, the velocity and stress at the node (x_m, z_n) are given by eqs (B1) and (B2). Substituting in eqs (19) to (25) yields eqs (B3) and (B4) but with the matrices Θ and Ψ given by

$$\Theta = \frac{1}{\rho}\begin{bmatrix} \sin(k_x h) & 0 & \sin(k_z h) \\ 0 & \sin(k_z h) & \sin(k_x h) \end{bmatrix} \tag{C1}$$

and

$$\Psi = \begin{bmatrix} \rho\alpha^2 \sin(k_x h) & \lambda \sin(k_z h) \\ \lambda \sin(k_x h) & \rho\alpha^2 \sin(k_z h) \\ \rho\beta^2 \sin(k_z h) & \rho\beta^2 \sin(k_x h) \end{bmatrix}. \tag{C2}$$

As in the previous appendix, the system is reduced to the second-order eigenvalue problem of eq. (B7), with

$$\Gamma = \alpha^2 \sin^2(k_x h) + \beta^2 \sin^2(k_z h), \tag{C3}$$

$$\Upsilon = \alpha^2 \sin^2(k_z h) + \beta^2 \sin^2(k_x h), \tag{C4}$$

$$\Phi = (\alpha^2 - \beta^2) \sin(k_x h) \sin(k_z h). \tag{C5}$$

The eigenvalues are given by

$$\Lambda_1 = \alpha^2 \left[\sin^2(k_x h) + \sin^2(k_z h)\right], \tag{C6}$$

$$\Lambda_2 = \beta^2 \left[\sin^2(k_x h) + \sin^2(k_z h)\right]. \tag{C7}$$

Finally, the grid dispersion relations are given by

$$\frac{\alpha_h}{\alpha} = \frac{1}{2\pi\delta_p}\sqrt{\sin^2\left(2\pi\delta_p \cos\theta\right) + \sin^2\left(2\pi\delta_p \sin\theta\right)}, \tag{C8}$$

$$\frac{\beta_h}{\alpha} = \frac{\epsilon}{2\pi\delta_s}\sqrt{\sin^2(2\pi\delta_s \cos\theta) + \sin^2(2\pi\delta_s \sin\theta)}. \tag{C9}$$

Comparing these grid-dispersion relations with those of SGFDM, eqs (B14) and (B15), it is clear that these two sets of equations are equivalent whenever the sampling ratios of SGFDM are double than those of VSFDM. Incidentally, the stability condition of VSFDM is precisely double than that of SGFDM; namely, the stability condition of VSFDM using a second-order finite-difference scheme for time stepping, is given by

$$\Delta_t \leq \sqrt{2}\frac{h}{\alpha}, \tag{C10}$$

where Δ_t is the size of the time step.

APPENDIX D: GRID-DISPERSION ANALYSIS OF THE SPECTRAL-ELEMENT METHOD

The grid dispersion of SEM for the acoustic and elastic cases has been analysed in De Basabe & Sen (2007) for up to order 10 basis functions, the analysis is summarized here for completeness. Their approach is an extension of the analysis developed in Cohen (2002), where the acoustic version of SEM is considered for basis functions up to order 3.

The analysis is based on the plane wave assumptions as in the finite-differences case. Furthermore, it will be assumed that the finite-element mesh is periodic, and that the elements are square with sides parallel to the coordinate axis and with tensor product basis functions; these are common assumptions whenever a FEM is analysed, see for example Marfurt (1984); Cohen (2002); Zyserman *et al.* (2003); Zyserman & Gauzellino (2004, 2005); Zyserman & Santos (2007); Ainsworth (2004a,b); Ainsworth *et al.* (2006); Seriani & Oliveira (2008); Gabriel *et al.* (2010). Introducing the assumption that the medium is homogeneous into the definitions of the mass and stiffness matrices (eqs 29–33) yields

$$\mathcal{M}_{ij} = \frac{1}{\alpha^2}\int_\Omega \phi_i \phi_j \, \mathrm{d}x \, \mathrm{d}z, \tag{D1}$$

$$\mathcal{K}^1_{ij} = \int_\Omega \phi_{i,x}\phi_{j,x} \, \mathrm{d}x \, \mathrm{d}z + \epsilon^2 \int_\Omega \phi_{i,z}\phi_{j,z} \, \mathrm{d}x \, \mathrm{d}z, \tag{D2}$$

$$\mathcal{K}^2_{ij} = (1-\epsilon^2)\int_\Omega \phi_{i,x}\phi_{j,z} \, \mathrm{d}x \, \mathrm{d}z, \tag{D3}$$

$$\mathcal{K}^3_{ij} = \mathcal{K}^2_{ji}, \tag{D4}$$

$$\mathcal{K}^4_{ij} = \epsilon^2 \int_\Omega \phi_{i,x}\phi_{j,x} \, \mathrm{d}x \, \mathrm{d}z + \int_\Omega \phi_{i,z}\phi_{j,z} \, \mathrm{d}x \, \mathrm{d}z. \tag{D5}$$

Assuming that the solution is a plane wave then U^x_j and U^z_j have the form (no summation over j)

$$U^x_j(t) = A_j e^{\mathrm{i}(\boldsymbol{k}\cdot\boldsymbol{x}_j - \omega t)} \quad \text{and} \quad U^z_j(t) = B_j e^{\mathrm{i}(\boldsymbol{k}\cdot\boldsymbol{x}_j - \omega t)}. \tag{D6}$$

Substituting in eqs (27) and (28), and neglecting the source term, yields

$$\Lambda\mathcal{M}_{ij}U^x_j = \mathcal{K}^1_{ij}U^x_j + \mathcal{K}^2_{ij}U^z_j \quad \text{and} \tag{D7}$$

$$\Lambda\mathcal{M}_{ij}U^z_j = \mathcal{K}^3_{ij}U^x_j + \mathcal{K}^4_{ij}U^z_j, \tag{D8}$$

where the eigenvalues are given by $\Lambda = \omega_h^2$. The above equations represent a generalized eigenvalue problem; It can be shown that the eigenvalues of the above system are real and positive (De Basabe & Sen 2007).

The order of the above eigenvalue problem can be very large since it includes all the nodes in the discretized domain, but it can be reduced to an eigenvalue problem of order proportional to the degrees of freedom in one element, this process is described in detail in Cohen (2002) and De Basabe & Sen (2007) (see also De Basabe & Sen 2010). The reduced-order eigenvalue problem uses the so-called dynamic mass and stiffness matrices which are computed using the wavenumber and are intrinsically related to plane-wave analysis. The procedure to compute these matrices takes full advantage of the structure of the tensor product basis functions and in order to do that the following notation is introduced to split the indexes of the matrices:

$$M_{ij} = M_{(i)(j_1,j_2)} \tag{D9}$$

where $j = \kappa j_2 + j_1$, $0 \leq j_1 < \kappa$ and κ is the polynomial degree of the basis functions on the sides of the elements. Notice that for every j there is a unique pair (j_1, j_2) and vice versa.

The dynamic mass and stiffness matrices are given by

$$\tilde{M}_{(i)(l_1,l_2)} = M_{(i)(\kappa q_1 + l_1, \kappa q_2 + l_2)} e^{k_x h q_1 + k_z h q_2}, \tag{D10}$$

$$\tilde{K}^\nu_{(i)(l_1,l_2)} = K^\nu_{(i)(\kappa q_1 + l_1, \kappa q_2 + l_2)} e^{k_x h q_1 + k_z h q_2}, \tag{D11}$$

for $0 \leq i < \kappa^2$ and $\nu = 1, \ldots, 4$, where $0 \leq l_1, l_2 < \kappa$. Note that summation is implied in the right-hand side over q_1 and q_2. The resulting eigenvalue problem is of order $2\kappa^2$. Using matrix notation, it is given by

$$\Lambda \begin{bmatrix} \widetilde{\mathcal{M}} & 0 \\ 0 & \widetilde{\mathcal{M}} \end{bmatrix} \begin{bmatrix} \boldsymbol{U}^x \\ \boldsymbol{U}^z \end{bmatrix} = \begin{bmatrix} \widetilde{\mathcal{K}}^1 & \widetilde{\mathcal{K}}^2 \\ \widetilde{\mathcal{K}}^3 & \widetilde{\mathcal{K}}^4 \end{bmatrix} \begin{bmatrix} \boldsymbol{U}^x \\ \boldsymbol{U}^z \end{bmatrix}. \tag{D12}$$

For high-order basis functions, the number of eigenvalues is large, but there are only two eigenvalues of interest for the grid-dispersion analysis, namely the ones corresponding to the *P*- and *S*-waves. In De Basabe & Sen (2007) we hypothesize that the eigenvalue corresponding to the *S*-wave is the smallest one, and the one corresponding to the *P*-wave is the second smallest and corroborate this hypothesis numerically. Finally, the grid-dispersion relations are given by

$$\frac{\alpha_h}{\alpha} = \frac{1}{2\pi\delta_p}\sqrt{\lambda_p}, \tag{D13}$$

$$\frac{\beta_h}{\alpha} = \frac{1}{2\pi\delta_s}\sqrt{\lambda_s}. \tag{D14}$$